RARE EARTH SILICIDES AS SOLAR CELL CONTACT MATERIALS

By

THOMAS DANTON BUSSING

A DISSERTATION PRESENTED TO THE GRADUATE SCHOOL
OF THE UNIVERSITY OF FLORIDA IN PARTIAL FULFILLMENT
OF THE REQUIREMENTS FOR THE DEGREE OF
DOCTOR OF PHILOSOPHY

UNIVERSITY OF FLORIDA

1991

This work is dedicated to

Henry George Bussing,

my late father, who taught me, and allowed me,

to think for myself.

ACKNOWLEDGEMENTS

I wish to thank Dr. Paul H. Holloway for his support, his patience and his prodding through the course of my post-graduate education.

The valued contributions of William Wresh, M.S., now with Texas Instruments, are gratefully acknowledged, particularly in the development of the codeposition process and for RBS analysis while with the department of Physics at the University of Florida. The assistance of Dr. Markku Leskela of the University of Turku, Finland, in the analysis of the x-ray diffraction data is also acknowledged.

I must mention without naming the numerous others who provided essential help and camaraderie: my colleagues and the staff of the department of Materials Science and Engineering, and the students and staff of the other departments at the University with whom I have worked. I thank you, one and all.

Last and most, I thank my parents for the gifts of love, patience and support that they have given me throughout my life and my continuing education, and I thank my wife Regina, whose support, patience, prodding, help, camaraderie and love made it possible to complete this work.

TABLE OF CONTENTS

ACKNOWLEDGEMENTS iii

LIST OF TABLES vi

LIST OF FIGURES viii

ABSTRACT xi

CHAPTERS

ONE — INTRODUCTION 1
Purpose 1
Overview 2
Silicides for Semiconductor Metallization . . 5
The Rare Earths 6
High Temperature Ohmic Contacts 7
Gadolinium as a Test Case 9

TWO — REVIEW OF LITERATURE 11
Metallization Requirements 11
Metal-Semiconductor Contacts 13
Schottky Barriers 13
Ohmic Contacts 17
Contact Resistance 21
Summary 25
Transition Metal Silicides 26
Formation and Reaction Kinetics 27
Silicide Properties 29
Rare Earth Silicides 34
Thin Film Reaction on Silicon 34
Rare Earth Contacts to GaAs 35
Resistivities 36
Problems with Reacted Thin Films 36
Crystallographic Structures of Rare Earth Silicides 37

THREE — DEPOSITION AND ANALYTICAL TECHNIQUES 45
Introduction 45
Thin Film Deposition 46
Analytical Instruments 50
Composition of Films 51

FOUR ANGLE-RESOLVED X-RAY PHOTOELECTRON SPECTROSCOPY (ARXPS) 55
Introduction 55
The Inverse Laplace Transform: An Iterative Solution 57
The ARXPS Flux Model 58
Example 1: Oxidized Silicon 60
Example 2: Sputter Altered Surfaces of (100) GaAs 62
Conclusion 65

FIVE QUANTITATIVE AUGER ELECTRON SPECTROSCOPY IN THE Gd-Si SYSTEM 74
Introduction 74
Experimental 75
Quantitative AES 76
Matrix-Corrected Sensitivity Factor S^{eff} . . . 80
Results and Discussion 86
Qualitative Results 86
Quantitative Results 88
Conclusion 91

SIX RESULTS OF ANALYSIS 101
Crystallization Behavior of Codeposited Films 101
X-ray Diffraction 101
Transmission Electron Microscopy 104
Metallurgical Stability 106
Stability/Reactivity of Films on Silicon 106
Stability/Reactivity of Films on GaAs 107
Effects of Oxygen 108
Oxygen Behavior in the Thin Film Reaction 108
Behavior of Oxygen in Codeposited Films 110
Electrical and Contact Properties 110
Resistivity 110
Contact Properties--Silicon (100) 111
Contact Properties--GaAs (100) 113
Problems in Patterning and Probing . . . 115
Optical Properties 116

SEVEN CONCLUSION 141

REFERENCE LIST 144

BIOGRAPHICAL SKETCH 152

LIST OF TABLES

Tables

2-1 Schottky barrier heights [in eV] of several rare earth disilicides to silicon. 41

2-2 Melting temperatures, $GdSi_2$. 41

2-3 Schottky barrier heights [in eV] of several rare earth metals to GaAs. 41

2-4 Bulk resistivities for rare earth silicides. . . 42

2-5 Thin film resistivities of rare earth silicides and rare earth metals 42

2-6 Unit cell dimensions for the three reported structures of $GdSi_x$ ($1.7 \leq x \leq 2$). 43

2-7 Anomalous densities for orthorhombic rare earth silicides. 43

4-1 Binding energy separation [in eV] of the peaks deconvoluted from the Si 2p XPS region 67

5-1 Atomic percent silicon and matrix correction factors. 93

5-2 Atomic percent gadolinium and matrix correction factors. 94

6-1 X-ray diffraction peak position (2θ) and d-spacing for 5,000Å $GdSi_2$ film after heat treatments. 118

6-2 Equivalent lattice planes and d-spacings, calculated for three structures of $GdSi_x$ . . . 118

6-3 Heats of formation for silicides. 119

6-4 Heats of formation for oxides. 119

6-5 Bond lengths: for orthorhombic $GdSi_{1.7}$, $ThSi_2$, and related disilicides. 120

Tables

6-6 Heats of formation and melting temperatures, rare earth arsenides. 120

6-7 Real and imaginary coefficients of the index of refraction measured for various silicides (λ=6328Å). 121

LIST OF FIGURES

Figure

2-1 Hexagonal and tetragonal lattices for $ThSi_2$. . . 44

3-1 Codeposition from a composite sputter target. . 53

3-2 RBS analysis of gadolinium disilicides 54

4-1 The geometry of the XPS analyzer. 68

4-2 Plot of signal intensity versus sample tilt angle for the Perkin Elmer PE5950 ESCA . . 69

4-3 Silicon 2p spectra from a silicon wafer with a native oxide layer. 70

4-4 Plot of relative silicon species intensities versus analysis depth $\lambda\sin(\theta)$ 71

4-5 ARXPS results for oxidized silicon wafers . . . 72

4-6 ARXPS results for the Ar^+ sputtered GaAs. . . . 73

5-1 Elastic backscattered beam (E_p = 2.8 keV). . . . 95

5-2 Effects of oxygen contamination on gadolinium silicide films [Si LVV/Gd NNN AES region] . . . 96

5-3 Si KLL AES region 97

5-4 AES composition of $GdSi_x$ versus RBS measurements. 98

5-5 Error factor after application of matrix correction terms, and empirical fit k'' 99

5-6 Comparison of high energy and low energy AES intensities 100

6-1 X-ray diffraction data 122

Figure

6-2 X-ray diffraction data for $GdSi_2$ film after rapid thermal annealing (RTA) 123

6-3 Juxtaposition of the hexagonal unit cell and the orthogonal/tetragonal half-unit cell . . . 124

6-4 Expanded view of x-ray diffraction data for $GdSi_2$ film after rapid thermal annealing . . . 125

6-5 X-ray diffraction data for $GdSi_2$ film after rapid thermal annealing (RTA) for different times 126

6-6 Expanded section of x-ray diffraction data for $GdSi_2$ film after rapid thermal annealing . 127

6-7 X-ray diffraction data for $GdSi_2$ film after furnace heat treatments (375°C, 30 min.) . . . 128

6-8 Planar TEM photos 129

6-9 Cross-sectional TEM of $GdSi_2$ film (800C° RTA anneal). 130

6-10 Cross-sectional TEM of $GdSi_2$ film (800°C RTA anneal). 131

6-11 Auger depth profiles of codeposited $GdSi_x$ films, x=2 (silicon-rich), showing change to 1.7:1 stoichiometry after annealing . . . 132

6-12 SEM photo of $GdSi_2$ film after furnace anneal at 900°C for one hour 133

6-13 Auger depth profiles of codeposited $GdSi_x$ films, x=2 (silicon-rich), on GaAs substrates . . . 134

6-14 Expanded view of Auger depth profile of annealed $GdSi_2$ film on GaAs 135

6-15 Auger line scan across the edge of a fixed ion-beam sputter crater in a partially-reacted Gd film on silicon. 136

6-16 Current-voltage measurements of $GdSi_2$ contacts on silicon. 137

6-17 Current-voltage data, $GdSi_2$ contacts on GaAs. 138

Figure

6-18 Optical reflectance of reacted $GdSi_{1.7}$ on Si substrate 139

6-19 Reflectance measurements of small (50 μm) spot size 140

Abstract of Dissertation Presented to the Graduate School of the University of Florida in Partial Fulfillment of the Requirements for the Degree of Doctor of Philosophy

RARE EARTH SILICIDES
AS SOLAR CELL CONTACT MATERIALS

By

Thomas Danton Bussing

May 1991

Chairperson: Dr. Paul H. Holloway
Major Department: Materials Science and Engineering

Silicides produced from a codeposited mixture of gadolinium and silicon have been studied as an alternative to the thin-film reaction method. Results include details of the composition, crystallographic structure and intrinsic properties of the films, electrical contact properties to silicon and gallium arsenide, and advancements in quantitative analysis of surface composition.

Rutherford backscattering spectroscopy (RBS) confirmed the reported temperature (350-400°C) of the thin-film reaction, and Auger electron spectroscopy (AES) depth profiles clarified the role of oxygen contamination in inhibiting the reaction.

For the codeposited films X-ray diffraction (XRD) showed progressive recrystallization at temperatures from 500-800°C, with strong preferred orientation effects and evidence of the

presence of the hexagonal phase as well as the expected orthorhombic phase in the recrystallized films. Auger depth profiles showed limited reaction with silicon or GaAs substrates during heat treatment, with an As-rich compound at the silicide/GaAs interface. Excess silicon was rejected from silicon-rich films to form the $GdSi_{1.7}$ compound. Resistivity of the films was 250μΩ-cm after heat treatment, and the Schottky barrier height to p-Si was 0.70eV.

A method of deriving a layered model of near-surface composition is presented, using the inverse Laplace transform of angle-resolved x-ray photoelectron spectroscopy (ARXPS) data. The inverse of a Laplace transform is not unique, and thus constraints are required to select a solution function. The new approach relaxes these constraints, allowing non-monotonic profiles to be recovered. Results are presented for an air-oxidized Si substrate demonstrating a layered surface oxide, with silicon-rich oxides at the SiO_2/Si interface. Ar-sputtered GaAs showed a surface enrichment of As above a Ga-rich layer, consistent with preferential sputtering by Gibbsian surface segregation of As.

Empirically derived AES correction factors are presented that permit accurate quantification of rare earth silicide films, correcting for effects ranging from surface segregation to changes in the effective attenuation length of the Auger electrons and backscatter effects.

CHAPTER ONE
INTRODUCTION

Purpose

Large scale implementation of photovoltaic power generation is dependent to a great extent on advances in materials and processing to achieve greater solar cell efficiency. The incentive is particularly strong in solar concentrator applications, where the marginal economic return is multiplicative compared to the cost of increased cell capacity.

The purpose of this study has been to evaluate the potential of rare earth silicides for improving solar cell performance. The role of the silicides would be to serve as a contact metallization layer, by which electrical current is passed into or out of the semiconductor solar cell material. Improvements in contact metallization can enhance concentration cell performance by reducing direct losses due to contact resistance and surface recombination of carriers. In addition, the service lifetime of the cells may be extended by enhanced metallurgical stability of the metal-semiconductor contact.

This means that an understanding of the electrical transport properties of the silicide and of the silicide-

semiconductor interface are of central importance to this study. To some extent these properties may be described by measurements of such parameters as the resistivity or thin film sheet resistance of the silicide, or the Schottky barrier height or specific contact resistance of contacts.

However, a full and complete characterization of the samples is as necessary to the study as the measurement of such device performance parameters. The actual sample morphology, the phases present, condition of surfaces and interfaces, and a host of other attributes may be expected to vary considerably with variations in preparation and treatment and can affect the response of samples to measurement.

Analysis of the deposited films has required the application of numerous techniques, and reconciliation of the results of the various techniques to give a full picture of the material under study. Fuller understanding of the data led to some of the significant results here presented, including the development of novel techniques in data reduction and corrections to standard analyses.

Overview

The effort to place this work properly in its context begins with a review of the literature. Chapter Two proceeds from a simple model of the metal-semiconductor junction to metallization requirements of semiconductor

devices in general, with models and analyses of several performance parameters, as an outline of the current technology. The chapter continues with a review of the basic properties of thin films of other metal silicides as a background for an introduction to previous work with rare earth silicides in the form of reacted thin films on silicon.

Chapter Three describes experimental work including fabrication of samples and fundamental thin film analysis to identify the disilicide phase. Early work involving the deposition of rare earth metals for reaction with silicon substrates provided samples for comparison with codeposited films, permitting the development of the ion beam sputter codeposition technique for gadolinium silicides.

Chapters Four and Five present examples of two areas in which a more in-depth approach to data analysis has been developed and demonstrated as necessary to enhance the accuracy of two commonly used analytical techniques for quantitative analysis of surfaces. Chemical composition as measured by electron spectroscopic analysis of a clean surface will often deviate from the bulk composition of a substrate or thick film. In Chapter Four it is shown that changes in near-surface composition may have a significant effect on the angular distribution of photoelectrons escaping the sample, with resultant nontrivial variations in the calculated relative abundance of the sample's elemental

constituents. It is further shown that from such measurements, taken at a series of angles of observation with respect to the sample surface, it is possible to derive layered models of the composition changes in a shallow region near the sample surface. In Chapter Five, correction factors are derived to permit accurate quantification of rare earth silicide films using Auger electron spectroscopy (AES). These empirically derived factors correct for effects ranging from surface segregation to changes in the effective attenuation length of the Auger electrons and backscatter effects.

In Chapter Six are the detailed results of analyses. Electrical contacts to both silicon and gallium arsenide have been studied, as well as the intrinsic physical, electrical and optical properties of the silicides. Strong crystallographic orientation effects were observed in the recrystallized films and are believed to play an important role in contact properties.

Chapter Seven presents a summary of the work and concluding remarks, with observations relevant to applications of these films and suggestions for future studies.

The balance of this chapter introduces the metal silicides as semiconductor contacts, and the rare earth elements and their silicides as interesting candidates for forming high-temperature stable Ohmic contacts.

Silicides for Semiconductor Metallization

Metal silicides have recently emerged as important contact materials for semiconductor applications, mainly as gates and interconnects in integrated circuit technology. Most of the progress has been realized using silicides of the transition metals, that is those elements in which valence electrons are being added to the 3d, 4d and 5d orbitals across the periodic chart. These silicides can be formed by reaction of a deposited metal layer with a silicon substrate at elevated temperatures. The silicide films formed in this reaction have advantages of good stability at high temperatures and stable interfaces with silicon.

Silicide films can also be formed by codeposition with annealing to form the silicide. Codeposited silicide films have found application in silicon technology and in GaAs devices.

The properties of transition metal silicides are summarized in Chapter Two. By virtue of the kinetics of their formation and properties, these metal silicides naturally fall into two classes, the refractory metal silicides (metals from groups IVB to VIB in the periodic chart) and the silicides of the noble and near-noble metals (group VIII).

The rare earth silicides form in a reaction that is highly exothermic and in many ways unique among the metal-silicon systems. They constitute an additional extensive

class of silicides with different reaction mechanisms, crystal structure and film morphology. However, their properties have been far less investigated.

The Rare Earths

The rare earth metals (i.e., the elements in the lanthanide sequence, from La to Lu) and their compounds often exhibit unusual properties[1,2] due to the uncommon electronic structure of these elements, with electrons being added to an inner 4f shell that is lower in energy than the bonding orbitals, 6s and 5d. These inner shell 4f electrons are well shielded and tend to be localized to their respective atoms. Rather than being continuously modified by the addition of valence-level electrons available for bonding, lanthanide chemical properties are to a large extent quite similar across the sequence. Chemical bonding involves only the 6s and 5d electrons common to all the elements, while the distinguishing electron from element to element is added to the more-tightly bound 4f shell.

This unusual electronic structure is responsible for unusual behavior such as the Lanthanide contraction, the decrease in atomic radius with the increasing effective nuclear charge across the series. These elements are comparable to magnesium in electropositive character and ease of oxidation. Removal of the valence electrons in compound formation produces a +3 oxidation state that is the

normal state for all of the lathanides, with the outermost remaining electrons being the distinguishing 4f shell.

Excitation of these 4f electrons requires considerable energy, and optical absorption in the visible range for rare earth compounds is unusual in that it tends to occur in sharp peaks similar to gas phase absorption rather than the broadened bands typical for condensed states. Mechanisms of electron transport by hopping between localized states are significant to the total conductivity of these compounds as well.[3]

Bonding is generally trivalent, involving the 6s and 5d orbitals that they all possess at the valence level. In addition to the lanthanides, yttrium and scandium are often included under the heading of "rare earths" because of their similarity to lanthanum as precursors in the IIIA column of the periodic chart.

High Temperature Ohmic Contacts

It is often desirable to inject current into or out of a semiconductor with a low power loss. Such a contact should ideally present a negligible barrier to current and thus should obey Ohm's law (the current should increase linearly with increasing voltage). The constant of this proportionality is a resistance attributed to the contact interface.

Metal silicides are generally known to be stable at high temperatures and can make ohmic contacts to semiconductors.[4,5] Previous work with reacted thin films of rare earth metals on silicon substrates has demonstrated that rare earth metal films will react with silicon at low temperatures (300-400C°) to form stable disilicides with extremely low Schottky barrier heights to n-Si.[6,7]

Ohmic contacts to n-type silicon are predictable from these low Schottky barrier heights, while contact properties to GaAs using these silicides have not been reported. Rare earth metals like other metals have higher Schottky barrier heights to n-GaAs, and silicide contacts may be expected to depend upon enhanced tunnelling or field emission to produce ohmic behavior.

Successful ohmic contacts to n-GaAs have rarely involved simple tunneling behavior through planar interfaces. Alloyed contacts, in which reaction with and consumption of portions of the GaAs substrate are believed to create a highly-doped surface layer, produce a nonplanar and inhomogeneous interface with alloy penetrations which increases the contribution of field emission to the current flow, as well as increases the effective area of the contact.[8]

Such an approach is limited at higher temperatures if continued diffusion and reaction lead to degraded contact properties or device failure. Rare earth silicides have the

potential for forming more abrupt and thermally stable interfaces to GaAs, while their ability to alloy and transfer dopants to the substrate may be limited. Thus they must depend heavily upon low barrier height and planar tunnelling for forming ohmic contacts to GaAs.

Gadolinium as a Test Case

The Lanthanide sequence has unique properties that tend to follow orderly trends across the periodic chart,[1] and if a property of one rare earth falls in an undesired range, one has reasonable hope that further up or down the series one may find an element that works. Gadolinium presents a good first choice for study, falling in the middle of the sequence. It has a 4f electron shell that is half-full with 7 electrons, which is a configuration of enhanced stability that affords some unique properties among the lanthanides. A search of the literature yields somewhat more information on the Gd/Si system than the other rare earth silicides.

The choice of Gd carries with it some advantages and some disadvantages. The lighter lanthanides ($Z<64$) are less attractive choices due to their higher reactivity with oxygen. However, some of the heavier lanthanides may offer greater potentials in that the hexagonal phase becomes more stable. There is evidence that this hexagonal phase may offer enhanced conductivity based on the results of Thompson et al.[9] This is a reasonable supposition in view of the

metal/silicon layered structure in the hexagonal phase. As the metal atoms decrease in size, the possibility of epitaxial growth of the hexagonal phase is also enhanced due to improved lattice matching with the Si(111) face. This match is optimized for $ErSi_2$.[10]

However, gadolinium falls on the borderline as far as stability of the orthorhombic/hexagonal phases, and has a demonstrated potential to grow epitaxially on either the (100) face[11,12] or the (111) face[13] of silicon. Among the rare earth silicides, it has the lowest barrier height to n-type silicon.[6,7] Gadolinium was therefore chosen as a particularly interesting element to study as a representative of the rare earth sequence.

CHAPTER TWO
REVIEW OF LITERATURE

Metallization Requirements

The role of metallizations can be seen in four basic applications. At the metal level in integrated circuit devices there are two functions, as gate or as interconnect metallizations. The MOSFET (metal oxide semiconductor field effect transistor) is controlled by a gate voltage which is applied to a metal electrode that is isolated from the substrate by a dielectric layer. This electrode and other device terminals are interconnected by a network of metal runners, called the device interconnect metallization. Current state-of-the-art devices use polysilicon (with a sheet resistance near 30-60 ohm/sq.) in both roles.[14]

In addition, current must enter or leave the semiconductor portions of a device through contacts, or metal-semiconductor interfaces, which can function as either a barrier (current-rectifying) contact or as an ohmic, low resistance (current-passing) contact.

The interest in silicides is based on the need to develop new metallization schemes for the microelectronics industry. Gates and interconnects are subject to increasingly stringent requirements as VLSI (very large

scale integrated circuit) developments lead to devices that are smaller in size, faster in response and consuming less power. Intrinsic RC delay due to high sheet resistance has placed a severe limit on the usefulness of polysilicon films as the conducting metallization.[15] As device size is reduced, fringe effects on gate capacitance begin to dominate and it becomes clear that the only potential for reducing the RC time constant is to reduce the sheet resistance term.[14]

On the other hand, most metals are subject to limitations in their stability under device processing or in the operating ambient. Whether the problem is low temperature reactions with the substrate or dielectric layer, low temperature melting or eutectic formation, high oxidation rate or susceptibility to electromigration, the list of choices among the low-sheet-resistance metals dwindles rapidly.[14] Thus a prime motivation is to provide alternative low-sheet-resistance conductors to enable the smaller device structures to reach their potential for faster switching speeds.

Contact applications are also affected by the size reduction in VLSI developments. Reduced junction depth means increased problems of metal penetration into silicon, especially for aluminum.[14] Silicides formed by reaction may have a similar disadvantage in that silicon is consumed in the reaction and shallow junctions may therefore be

penetrated. But silicides that are codeposited as a mixture can minimize the substrate reaction, and are expected to be more stable over shallow junctions.[16,17,18]

Metal-Semiconductor Contacts

Schottky Barriers

The simplest model of a metal-semiconductor interfacial barrier to current is the Schottky barrier model. In this model the Fermi energy of the metal and the semiconductor are equalized by a transfer of charge at the interface, resulting in a dipole electric field at the interface.[19] The metal carries a charge at its surface, while the semiconductor distributes an equivalent but opposite charge across a finite layer known as a space charge region, equivalent to that formed at a semiconductor n-p junction. Since the majority carriers are opposed to the charge developed, they are depleted in number within the space-charge region, which is therefore also referred to as the "depleted" region.

The charge imbalance at the interface acts as a potential barrier to the flow of carriers across the interface, and a rectifying contact results. Charge transport under forward bias is governed by the process of thermionic emission, with only those carriers having adequate thermal energy to cross the barrier available to carry the current. The current density across a Schottky

barrier of height ϕ_B with applied voltage V is governed by the equation

$$J = A^{**}T^2 \left[\exp\left(\frac{-q\phi_B}{kT}\right)\right] \left[\exp\left(\frac{qV}{nkT}-1\right)\right] \qquad (2\text{-}1)$$

where A^{**} is Richardson's constant, k is Boltzmann's constant, T is the temperature (Kelvin), and n is the "ideality" factor, which is unity for ideal Schottky contacts.

According to this equation a plot of the logarithm of the current versus applied voltage should be linear, with the barrier height derivable from the zero-voltage intercept. This approach is commonly used to measure Schottky barrier heights, assuming an abrupt, planar interface between a semiconductor substrate and a uniform metal layer. However, even with elemental metal films on elemental substrates this is not always the case and is increasingly unlikely with compound films and/or compound substrates.[20]

Schottky barrier height and work function

In the pure Schottky model, the Schottky barrier height is defined as the difference between the electron affinity of the semiconductor and the work function of the metal. The work function of a material is difficult to measure accurately, but it has been pointed out that the work function is related to the electronegativity of a metal,[21]

which is a measure of its tendency to acquire an additional electron. Plots of barrier height against either quantity show reasonable agreement with the theory. For a given elemental or compound semiconductor, barrier height is dependent upon the ionicity of the bonds in the semiconductor.[22]

The Bardeen model

Real contacts rarely exhibit ideal Schottky behavior. Surface electron states due to defects (such as unsatisfied bonds in the terminated semiconductor lattice or contamination of the interface) can produce departures from the expected or "ideal" barrier height.[23] These surface states, occurring at forbidden energies in the semiconductor band gap, are capable of compensating the charge of the metal, which in turn pins the Fermi level of the semiconductor surface at the level of the filled traps. This results in a barrier height that is independent of the metal work function. While for silicon either model has application, for the case of compound semiconductors such as GaAs, the Bardeen model is necessary to explain this observed independence of barrier height from the metal work function.

Schottky barriers of metal silicides

For the reacted silicides, the scavenging effect of the silicide formation leads to an interface that is relatively free of imperfections and contamination. For this reason,

reliable and reproducible Schottky barrier contacts are readily achieved using silicide reactions.[24] Devices with invariant contact properties and a range of barrier heights are produced in this fashion.

Barrier heights for the silicides are not far in value from those of the metals themselves and have been plotted relative to the metal work function with reasonable agreement to linearity, although the silicon-rich silicides tend to have lower barrier heights than other silicides and less dependence on the work function of the metal.[25] Plots against a weighted average work function using an arbitrary hypothetical interfacial composition do not yield improved results.[26]

The relation of barrier height to work function is not totally satisfactory, and other correlations are observable.[5] Many transition metals sharing a high affinity for oxygen (groups IVB-VIB) exhibit a barrier height near half the silicon band gap. Metals in group VIII have little affinity for oxygen and barrier heights that are high and increasing with the number of d-electrons.

Other approaches taken involve thermodynamic considerations that can be related to electronegativity and the work function, such as the heat of formation of the silicide,[27] or eutectic temperatures from the binary phase diagrams.[28] The first approach predicts no barrier higher than 0.83eV, which fails for PtSi and IrSi.[24] The latter

approach involves choosing the temperature of that eutectic composition (in the silicon-metal binary phase diagram) which is closest to the side of the dominant diffusing species in the silicide-forming reaction and is reasonably successful. It is postulated that the properties of the reactive interface are dominated by an interfacial layer of a eutectic composition, which is energetically favored to form when the appropriate composition is reached at the interface due to the interdiffusion of the two species. It has been suggested that a low Schottky barrier height is related to the eutectic temperature of the silicide, with a decreasing barrier height associated with increasing eutectic temperature.

Ohmic Contacts

The simplest model for the establishment of an ohmic contact to a semiconductor is the Schottky-limited model, where the contact is a simple junction between the semiconductor and a metal that has a work function closely matched to the semiconductor conduction band-edge (for n-type), or the valence band-edge (for p-type). A work function slightly above (or below) the band edges of the semiconductor causes an accumulation rather than a depletion of carriers, which presents no barrier to current flow for either the n-type (or the p-type) semiconductor.[29] A metal having a work function within the band gap, but near a band

edge, has a very low Schottky barrier height to that particular band, with the contact closely approaching ohmic behavior.

In actuality it is found that metals of suitable work function are seldom available or practical in application, even if Fermi level pinning were not found to play a dominant part in barrier creation. However, ohmic behavior can still be approached if a high carrier density is present at the surface of the semiconductor, thus creating a very narrow space-charge region which can be penetrated by tunneling of the carriers.[30]

Thus formation of practical ohmic contacts of low contact resistance is generally achieved by forming a highly doped layer in the semiconductor in contact with the metal.[31] Higher doping levels in the semiconductor cause a narrowing and lowering of the potential barrier. The space charge region is made narrower because the increased dopant concentration allows charge balance to be achieved over a shorter distance (expressed as shortening of the Debye length, the characteristic distance over which a charge imbalance is dissipated in the semiconductor). In addition, the barrier height is lowered due to image force effects (charge redistribution when a carrier approaches the barrier). The narrower and lower the barrier, the greater the probability of quantum mechanical tunneling, and increased tunneling of carriers is often used to produce

contacts that are effectively ohmic, with tunneling as the dominant conduction mechanism.

This is practically realized by a number of approaches. Some depend upon the formation of a low-melting eutectic interfacial phase in a metallurgical reaction that consumes portions of the semiconductor. In some cases a highly doped surface layer of the semiconductor recrystallizes from the molten eutectic (e.g., Al/Si).[32] Others depend on the indiffusion of a dopant from the metal layer during the reaction. In the case of n-GaAs, ohmic contacts have been achieved using a Au-Ge or Ni-Au-Ge alloy. It is hypothesized[33] that a liquid phase eutectic is formed at the interface during heat treatment, with Ga outdiffusion into the liquid permitting Ge to penetrate the GaAs lattice and occupy the empty Ga sites. This creates an n^+ surface layer and a sharply defined space-charge region, with tunneling through the barrier as the major mechanism of charge transport at the interface.

Devices using contacts that are based on reactive metallurgy often fail due to excessive reaction between the semiconductor and the metal layer.[34,35] Whether it takes the form of "spiking" (penetrations of reacting metal into the semiconductor, sometimes to the cell junction causing a junction short), or recombinative poisoning by electrically active metal atoms diffusing into the semiconductor, these contacts are subject to failure in processing and in the

field. The very reactivity that activates these contacts is capable of corrupting them. The dependence on these reactions can be avoided by preparing a substrate with a highly doped ion-implanted or grown surface layer, and using a metal that is unreactive with the substrate.

Special application--solar cells

In developing a solar cell metallization scheme, there are a handful of criteria that can be decisive in satisfying the question of its usefulness: 1. acceptable cost, 2. low contact resistance, 3. low sheet resistance, 4. stability in processing (including heat treatments), and 5. durability in service.

For concentrator applications, a higher cost may be acceptable, but a lower contact resistance and a lower sheet resistance of the metal are desired because of the higher current densities that must be handled by the cell metallization.[36] Thus, multilayer structures are commonly used, with a contact layer providing a good ohmic contact to the semiconductor as well as a diffusion barrier that should provide good adhesion for a thick conducting overlayer.

Metal Silicides for ohmic contacts

With a stable interface to silicon, and assurance of reduced junction penetration by using codeposited silicides or silicon-metal mixtures, silicides have the potential for forming contacts of low resistance, particularly in the case of the near-noble metal silicides.[37,38] The barrier height

can be reduced dramatically by controlling the surface doping of the semiconductor,[19] and ohmic contacts should be readily achievable for most of these silicides, especially the noble metal silicides on p-silicon.

Metal silicides exhibit several properties that recommend them as candidates for forming stable ohmic contacts; they have good high temperature stability and can form stable interfaces of low contact resistance to silicon. They have further potential application as contacts to gallium arsenide if their reactivity with the gallium arsenide is limited.

Contact Resistance

Once an ohmic contact is achieved, a criterion of quality is a low resistance to the passage of current. Specific contact resistance (ohms-cm^2) is defined as the resistance of a unit area of the metal-semiconductor interfacial layer.[39] Contact resistance is a strong function of the doping level of the semiconductor, which is reasonable in that the Schottky barrier height and Debye length are sensitive to the carrier concentration.[19] Thus there is great potential in processing for optimizing the contact resistance of tunneling ohmic contacts.

The transmission line model (TLM) of the metal-semiconductor contact introduced by Shockley and refined by Berger[40] is used in a common method of measuring specific

contact resistance. Measurements on a test structure consistent with the model permit the evaluation of a transfer length, which in effect expresses the contribution of the contact resistance to the total resistance of the test structure as equivalent to an additional length of substrate.

Contact resistance may also be given in units of line resistance (ohm-mm). This "front" resistance gives the interfacial resistance in terms of the width of the contact and is equivalent to the product of a transfer length and a sheet resistance of the substrate. It is evaluated directly from the measurements and thus incorporates any changes in the substrate resistivity due to formation of the contact.

Contact resistance measurement

The transmission line model (TLM) allows the calculation of specific contact resistance based upon measurements of voltage and current across a suitable test structure.[40] The structure generally used consists of rectangular contact bars of width W, with a length L and a spacing S along the current-carrying axis. Conduction is restricted to a thin diffused or doped surface layer of thickness t (t=0.3-1.0 microns), by creating a junction potential barrier that prevents carriers in the bulk of the substrate from participating in the charge transport. The model requires that S>>t, W>>L, and that current spreading beyond the pattern be negligible.

Correct measurements to accurately separate the contact resistance from the other resistances in the TLM structure are not always straightforward. Accurate measurement of very low-resistance contacts is difficult. Probe placement may have an undesirable effect, particularly for the case of a more highly resistive film, and the "front" and "end" contact resistances may be confused. Measurements necessarily include both forward- and reverse-biased contacts, which for marginal contacts can have the effect of exaggerating the forward resistance of interest for solar cell applications. Also, the sheet resistance of the substrate may be altered beneath the contacts due to reactions in forming the contact (e.g., scavenging some thickness of the semiconductor, doping by diffusion, creating Auger recombination centers), the effects of which are not accounted for in this model.

Other test structures

Meier and Schroder[41] presented another structure consisting of an array of narrow parallel bars (n=40), in which the effects of contact resistance are accumulated over the pattern, which reduces the effects of current and voltage probes. In addition, this model allows for the sheet resistance of the substrate under the contact bars to be different from the sheet resistance between the bars.

A four-terminal Kelvin resistance test structure[39,42] allows the direct measurement of interfacial contact

resistance, obviating the need to evaluate a transfer length which is small compared to the other terms involved.

Limitations

Modeling the current flow in various test structures shows that contact resistance measurements may vary considerably due to a variety of factors, some geometric and some related to sample properties;[43] attaching a clear meaning to a particular measurement is not at all straightforward.

The test structure should resemble the device geometry in order for the measurement to be an appropriate assessment of contact resistance for that application. The Kelvin test structure referred to above is capable of determining very low contact resistances, but it also measures a current passing through a plane of contact and thus reduces edge effects. However, for the application at hand as a top-contact for solar cells, current-crowding[44] at the edge of the contact due to the predominately horizontal flow of the current is expected to dominate the device. In addition, since losses due to contact resistance are expected to be on the order of 0.5% of the power loss, practical contact resistances need not be as low as those that necessitate the Kelvin measurement.

Measurements using the TLM model depend upon the conductance of the metal film being very much greater than that of the substrate, and furthermore that the current

carried in substrate be confined to a thin surface layer, modelled as a transmission line. For more resistive metals, the first requirement (i.e., that the conductance be higher than that of the substrate) would call for a thinner or more lightly doped conducting layer. Reducing the doping makes ohmic contact more difficult to achieve, while thinning the conducting region becomes impractical and fringe field effects begin to contribute as the substrate p-n junction becomes sizeable compared to the surface conducting zone.

All of these measurements require a homogeneous interfacial layer to produce meaningful results;[42] sintered Al-Si contacts have been shown to exhibit uneven reaction near the edges of the contact with the formation of excessive eutectic reaction product, and contact resistance measurements with various sizes of contact bar show nonlinear properties consistent with this edge effect. If uniform contacts are not achieved, an accurate estimate of the interfacial contact resistance cannot be made.

Summary

In semiconductor device applications, silicides offer many candidates with low and metal-like resistivities and high temperature stability. They are also expected to have good resistance to electromigration due to the strong bonding compared to metals, and if formed on polysilicon they can be useful in providing lower resistance within the current MOS gate technology.

The material properties of interest are many, but of greatest importance to device design are sheet resistance, Schottky barrier height and contact resistance. For stability in processing and device reliability, films must be stable with respect to the substrate and dielectric layers under thermal cycling and have tolerable oxidization behavior. Physical properties of films such as stress, smoothness and adherence, and etchability for patterning are also of concern. The properties of transition metal silicides are discussed below.

Transition Metal Silicides

Two classes of transition metal silicides have emerged as the most interesting for semiconductor applications: the refractory metal silicides (metals from groups IVB to VIB in the periodic chart) and the silicides of the noble and near-noble metals (group VIII).

The near-noble and noble metals are so named because they exhibit little or no affinity for oxygen, while the refractory metals have high melting temperatures and are thus often suited for refractory (high temperature) applications. The two classes of silicides are clearly differentiated in terms of the temperature, mechanism and dominant diffusing species in the thin film reaction on silicon substrates.

They also display characteristic differences in terms of the properties of the silicide formed and its interfacial

electronic properties with respect to silicon. While the similarities within each class are thus emphasized, it is to be noted that there are exceptions, as well as properties that vary significantly, and not always in a well-behaved fashion, within each class or column of the periodic table.

Formation and Reaction Kinetics

For metal films on silicon or polysilicon substrates, the metal-rich phases are often formed first, frequently consuming all of the metal before the appearance of a phase richer in silicon.[5] The final phase is generally near M:Si::1:2 at higher temperatures and in the presence of excess silicon, which is typical of the processing environment for silicon devices. This superior stability of the dominant phase once formed on silicon is advantageous from the point of view of device processing.

Studies of the time dependence of silicide growth in most cases indicate a $t^{1/2}$ dependence, indicating a diffusion-controlled reaction.[14] In other cases, sometimes in the same system, a linear time dependence was observed, indicating an interface rate-controlled reaction, raising the questions of surface cleanliness and clearly leaving the question open for further study.

In any case, the refractory metals react at elevated temperatures (T>600°C), and silicon is the dominant diffusing species, while for the near-noble metals the

reaction temperature is lower (T<600°C), but the metal atoms are found to dominate the diffusion and perhaps promote the breaking of the Si-Si bonds at the low temperatures due to their interstitial migration.[45]

The tendency for the reactions to proceed to the formation of silicon-rich phases can be understood thermodynamically, in that the heat of formation per metal atom increases with increasing silicon content, with a disilicide forming a two-phase field with silicon at the silicon-rich end of the binary phase diagram.[14] However, efforts to formulate rules accurately predicting first-phase formation and second-phase nucleation from phase diagram parameters have not been totally successful. Factors affecting first phase formation include cleanliness of the interface, purity of materials, diffusivity, relative free energy of formation and temperature of interaction. It should be noted that the presence of an oxide on the interface can have serious effects on the reaction, even for metals with low affinity for oxygen.[14]

For the refractory metal silicides, the crystal structures of the final silicon-rich phases follow a trend across each period in the chart,[5] from orthorhombic (group IV) to hexagonal (group V) to tetragonal (group VI). The near noble metals are more disparate, from cubic for the third period (Co, Ni) to hexagonal (Pd) and orthorhombic (Pt).

Codeposited silicides are generally amorphous as deposited. On silicon or polysilicon they nucleate in the disilicide phase, with rejection of excess silicon or reaction with the substrate to form single-phase disilicide. On oxide, they tend to form a phase mixture according to the composition deposited.[46]

Silicide Properties

Physical properties

Films produced by the thin film reaction are potentially subject to a large tensile stress, due to the large net volume shrinkage resulting from silicide formation.[14] The relatively open silicon lattice is capable of accommodating a large portion of the volume of metal atoms introduced in the formation of the silicide. Stress can threaten the mechanical stability and even in cases the adhesion of films.

However, while the films do show tensile stress at room temperature after high temperature annealing, it is much less than would be expected from the volumetric change of the reaction. It is comparable to the stress level of annealed codeposited stoichiometric films,[14] $1x10^{10}$ to $2x10^{10}$ dyn/cm^2.

The stress in codeposited films often shows a marked dependence on the Si/metal ratio.[47] Codeposited films of correct or silicon-rich stoichiometries tend to have low

stress as deposited, but annealing produces tensile stresses in these films as well, apparently due to differences in thermal-expansion coefficients with respect to silicon substrates.[48]

The details of stress development vary among these metals. Ti and Ta films are compressive as deposited, but with annealing develop tensile stress which levels off at high temperatures.[49] Co films are in tension as deposited, and with reaction this tension increases, then is reduced after peaking at 900°C[5]. For Pt and Pd films the stress is low and tensile as deposited, increasing with annealing temperature, and leveling off or decreasing above 700°C.[50] Ni films have a very low tensile stress that increases slightly with temperature. This low stress may be related to the growth of epitaxial $NiSi_2$ on silicon, which is observed in these films.[51,52]

For $TaSi_2$, $TiSi_2$, $MoSi_2$ and WSi_2, the silicides show no hysteresis in stress as a function of temperature in situ in both the heating and cooling cycles, which indicates stability once formed.[48]

The silicides show good adhesion for the stable silicide. However, at temperatures of 500° and 600°C, Ni films and Co films (thicker than 100nm) form a monosilicide which lifts off the substrate.[5]

Etchability

Etching of silicides is problematical. Wet chemical etching is generally ineffective except in HF, and the HF

will attack silicon and SiO_2 structures in the device as well. In the lack of selective chemical etchants, the choices are narrowed to 1) chemically etching a pattern into a deposited metal before annealing to form the silicide, 2) lift-off of a patterned resist, or 3) reactive ion etching (RIE). Developments in the latter have the most long-range promise.[14]

Oxidation behavior

Device processing often involves oxidation steps to grow an insulating layer of SiO_2 on the exposed silicon. The silicides should survive these oxidation treatments, and hopefully would be capable of producing a dielectric layer on the silicide as well. Lastly, metallizations must be stable on SiO_2 layers during heat treatments.

Oxides of the metals show melting points that decrease from group IVB to VIB, and increase with each period.[5] Thus of group VIB only WO_3 has a melting temperature above 1000°C, and only those in group VB heavier than V meet this test.

Volumetric change in the metals upon oxidation also do not favor group VIB, with the metals exhibiting a much larger percent volume gain compared with SiO_2, which would produce large accommodating stresses upon oxidation. Groups IVB falls below SiO_2, and group VB slightly above, with respect to expansion in oxidation.[5]

A comparison of the heats of formation of metal oxides versus that for SiO_2 shows that for group VIB metals, the

oxides are less stable than SiO_2 and therefore oxides of Cr, Mo and W can be reduced by Si. Under oxidation in the presence of excess silicon, silicides of these metals will be stable; when there is no excess silicon available, they will tend to lose silicon to the oxide and become metal-rich.[5]

Group IVB metals can reduce SiO_2, and to a lesser degree so can the group VB. Silicides of these elements may form both oxides. For other transition metals, as for the group IVB, oxidation of the metal in preference to the silicon can lead to decomposition of the silicide, with a buildup of silicon residue.[5]

Experimental results in general concur with this thermodynamic picture. An SiO_2 cap grows on silicides that have an intervening layer of polysilicon between the silicide and an underlying oxide, and the polysilicon is consumed without affecting the silicide, except for $MoSi_2$ and WSi_2 films, which as expected become metal-rich under the SiO_2 cap.[14] For silicides directly on the oxide, $TiSi_2$ and $TaSi_2$ are reasonably stable; again $MoSi_2$ and WSi_2 are unstable, producing metal-rich films, metal in the films, and evolving volatile metal oxides. For gate electrodes only silicides such as those of Ta and Ti seem recommended.

Sheet resistance

A great deal of the interest in silicides is due to their low resistivity with respect to conventional

polysilicon gate metallizations. Silicides of the transition elements vary from near 15μΩcm. to over 1000μΩcm. in resistivity.[14] For thin films, resistivities are generally higher than bulk values, but a number of reacted silicides have been reported in the promising range of 40-60μΩcm. Codeposited films are generally more resistive than reacted films of the same element.

For the silicides formed from metals of group IVB to VIIB of the periodic table, it has been observed that in a given period an increase in resistivity is observed with increasing number of d-electrons. This change is associated with a change in the crystal structure, from orthogonal to hexagonal to tetragonal, and both changes are attributable to the changing electronic structure of the metal atom. It has been speculated that the very low resistivity of the group IVB metal silicides is related to a hybridization of the two d-electrons with s-p electrons from the silicon.[53,54] With increasing metal atom size, the periodic change is less pronounced, and for group VIII elements the resistivity is low and relatively constant.

By comparison, the resistivity of the transition metals themselves tends to decrease across each row, with an anomalous peak at group VIIB attributed to the very stable d^5 configuration, and group VIII metals, like the silicides, have low resistances that are similar in value.

Rare Earth Silicides

The thin film reaction of a silicon substrate with a deposited rare earth metal produces a stable and homogeneous disilicide film with a very low Schottky barrier height to n-silicon[6,7] (0.3-0.4 eV) [Table 2-1]. These low barriers suggest that low-resistance ohmic contacts may be achieved with electron tunneling as a dominant conduction mechanism. Given their high melting temperatures[55,56] [Table 2-2] the rare earth silicides are clearly excellent candidates for low resistivity, thermally stable contacts for n-Si.

Thin Film Reaction on Silicon

The rate of the rare earth-silicon reaction is difficult to determine due to the extreme rapidity with which the metal is consumed.[45] Using ion-beam-induced mixing[57] or rapid electron-beam pulses to dissolve interfacial impurities[58] permitted measurement of the activation energy for erbium-silicon (E_a=1.75 eV) and Tb-Si (E_a=1.6 eV) reactions. Thus, even at the very low temperatures at which the reaction is initiated through the interfacial barrier, rates of formation of the silicide are rapid. The result is the rough and pitted surface that is typical of the rare earth/silicon thin film reaction.[9,59,60]

In addition, it has been pointed out that rare earth disilicides can form a hexagonal phase (AlB_2 type) with a [0001] face that is closely related to the (111) face of

silicon.[10] Epitaxial thin films have been demonstrated for the higher lanthanides (Z>63) using rapid anneals by electron beam or laser.[11,12] Epitaxy of the orthorhombic "$GdSi_2$" allomorph on Si(100) has also been reported.[13] Such epitaxial layers may offer potential advantages in interface stability and properties, for example enhanced resistance to diffusion (i.e. diffusion barriers) if penetration of the silicide by conductive overlayers is reduced by the elimination of grain boundaries.

Rare Earth Contacts to GaAs

Rare earth silicide contacts to GaAs have not been reported. However, photoemission studies of several rare earth metals on cleaved GaAs(110)[61-65] show room temperature reaction resulting in an abrupt interface and Fermi-level pinning in the bandgap [Table 2-3].

The nature of Schottky barrier formation continues to be controversial,[66] with schools supporting the roles of defect states,[67,68] chemical reactivity and effective work function of interfacial compounds,[69] and strength of the chemical bond and its dipole[70] as factors in the pinning behavior. The high reactivity and low electronegativity of the rare earth metals makes them good test cases for these divergent theories, but the barrier heights measured do not show agreement beyond the expected band-gap pinning.

In so far as the barrier height of the silicide will follow that of the metal, and given the inevitable pinning

in the band gap for GaAs, successful Ohmic contacts will depend upon tunneling or thermionic field emission as dominant conduction mechanisms. Calculations have shown that these mechanisms can produce low contact resistances on highly doped ($n_D \geq 10^{18}$ cm^{-3}) substrates,[30] with exponential decrease in R_c with decreasing barrier height. Thus the discrepancy in barrier heights reported for rare earth metals [see Table 2-3] would translate to a factor of 5 to 10 in contact resistance for tunneling Ohmic contacts. This underscores the significance of these barrier height measurements for Ohmic contacts.

Resistivities

Bulk and thin film measurements show moderate resistivities for the rare earth silicides[9,56,71] [Table 2-4, 2-5], which indicates that they will be better suited to multilevel metallization schemes with a more conductive metallization layer. Interestingly, semiconducting properties and a band gap of 0.19 eV have been reported for $LaSi_2$.[72,73] If this were true of other silicides it would have implications for performance in devices.

Problems with Reacted Thin Films

The main problems encountered in the previous studies of reacted thin films on silicon are related to oxygen contamination, either incorporated oxygen in the deposited

rare earth metal or surface oxides on the silicon substrate, which are dissolved by the strongly-reducing rare earth metal. High concentrations of oxygen in the metal inhibit the onset of the silicide reaction, and have been also been identified as the cause of the extreme roughness of the resulting films, due to rapid reaction beginning at points of weakness in an oxide barrier layer.[74]

This pitting has been identified as a factor in poor diode behavior and is undesirable for the fabrication of shallow contacts.[75] The pitting has been reduced or eliminated by ion-implantation or mixing,[57] rapid annealing by electron beam[76] or halogen lamp,[12] codeposition of metal-silicon mixtures,[77] UHV deposition on atomically clean surfaces,[78] or by prereaction of very thin metal films before depositing the desired thickness of rare earth metal.[79]

Crystallographic Structures of Rare Earth Silicides

Rare earth silicides near the disilicide composition may exhibit several crystal structures, depending upon temperature, composition, size of the metal atom, and valency of the compound.[80] The complexity of rare earth crystallography makes phase identification difficult for these films.[59]

Gadolinium with its characteristic orthorhombic "$GdSi_2$" structure lies at the crossing point of tendencies to form

tetragonal $ThSi_2$-type structures (lower lanthanides) or to form hexagonal structures of AlB_2-type or a silicon-deficient "defect" AlB_2 (higher lanthanides).[81]

The hexagonal lattice can be arrived at by a small distance shift of a few atoms along the [010] direction of the tetragonal lattice[82] [Figure 2-1], which can explain the reversible temperature-dependent transformation observed in these compounds.[83,84,85] The hexagonal form is favored at lower temperatures, low silicon content, and low population of free electrons (low valency), as well as low atomic size (higher atomic number). The orthorhombic "$GdSi_2$" distortion of the tetragonal lattice is an intermediate form, also characterized by a deficiency in silicon and intermediate atomic size ratio ($r_{Si}/r_M \approx 0.58$).[81] At higher temperatures the tetragonal $ThSi_2$-type structure has also been reported for Gd and other rare earths[82,86,87] [Table 2-6].

Both the orthorhombic and the hexagonal forms have been observed in reacted films of rare earth silicides,[59] although Gd favors the orthorhombic form both in bulk[83] and thin film samples.[9] An exception is found for liquid-phase reaction of Gd films on Si(111) by electron-beam melting.[11,12] Hexagonal $GdSi_{1.7}$ has been also been formed in bulk samples using a low-temperature amalgam method ($T<600°C$)[81] or by higher temperature reaction of silicon-deficient mixtures.[87]

The hexagonal form of disilicide exhibits two distinct AlB_2-type structures for the actinide and lanthanide metals,

one stoichiometric and the other deficient in silicon.[82] For the silicon atoms to fit perfectly into interstitial sites in a hexagonal AlB_2 structure requires a low size ratio of the metal atom to the silicon atom ($r_{Si}/r_M \leq 0.527$). Since these compounds that do not satisfy the size ratio requirement for ideal interstitial configuration, they form a defect AlB_2 structure in which the unit hexagonal cell must expand in either the [0001] or the [1000] direction. Stoichiometric compounds follow the latter arrangement, and as a result the axial ratio of the cell c/a is less than unity (i.e., for ideal interstitial AlB_2, c/a = 1). For nonstoichiometric or defect AlB_2 structures, the expansion is in the axial direction, so that c/a > 1.

The rare earth silicides form the AlB_2-type structure only when the atomic size ratio r_{Si}/r_M is greater than 0.579, well above the required ratio for interstitial arrangement ($r_{Si}/r_M \leq 0.527$). These compounds exhibit an axial expansion of the unit cell, and a tendency to be nonstoichiometric. Thus Gd_3Si_5, in the hexagonal form, has axial ratio c/a = 1.076.[87] Since disilicides of Tm and Yb have been observed to maintain this structure even at 2:1 stoichiometry,[84] it appears that the alternative radially expanded AlB_2 lattice does not occur for the rare earth silicides.

For the orthorhombic "$GdSi_2$" form, considerable deviation from stoichiometry has been observed in bulk samples. Perri et al.[86] found that both density

measurements and X-ray intensity analysis indicated that the stoichiometry was $GdSi_{1.4}$, and lower density has also been found[56] for the orthorhombic $DySi_2$ [Table 2-7]. More recent RBS studies of orthorhombic-phase $GdSi_x$ thin films indicate stoichiometry from 1.4:1 to 2:1, a considerable range of homogeneity, with stable properties beginning at $GdSi_{1.7}$.[77] There remains potential confusion concerning this point because many studies seem to rely on measurements of the hexagonal AlB_2 phase which is also commonly assigned a ratio of 1.7:1.[88] In this study, reacted products of stoichiometry 1.7:1 were chosen as the baseline for composition.

Table 2-1 Schottky barrier heights [in eV] of several rare earth disilicides to silicon.

	YSi_2	$GdSi_2$	$DySi_2$	$HoSi_2$	$ErSi_2$	ref.
n-Si	0.39	0.37	0.37	0.37	0.39	6
p-Si	-- 0.75	0.71 --	0.73 --	-- --	0.70 0.77	6 7

Table 2-2 Melting temperatures, $GdSi_2$.

Compound	T_m, C°	ref.
$GdSi_2$	1500	55
$GdSi_2$	1540	56

Table 2-3 Schottky barrier heights [in eV] of several rare earth metals to GaAs.

Metal	Φ_b	ref.
Sm	0.63	64
Tb	0.85	61
Dy	0.85	61
Er	0.85	61
Yb	0.61- 0.72	65

Table 2-4 Bulk resistivities for rare earth silicides.

Silicide	R_o [μΩcm.]	ref.
$ScSi_{1.6}$	40.6	71
YSi_2	69.0	71
$LaSi_2$	350.0 273	71 56
$CeSi_2$	183.0	71
$NdSi_2$	349	56
$SmSi_2$	210.0	71
$GdSi_2$	263	56

Table 2-5 Thin film resistivities of rare earth silicides and rare earth metals, and bulk resistivities of the metals, based on Table I., ref. 9.

Metal	Y	La	Gd	Dy	Ho	Er
Thin film R_o, μΩcm.	95	104	133	116	99	81
Bulk R_o, μΩcm.	60.2	79.4	135.9	92.6	80.6	85.5
Silicide	YSi_2	$LaSi_2$	$GdSi_2$	$DySi_2$	$HoSi_2$	$ErSi_2$
R_o, μΩcm.	135	116	207	204	185	115

Table 2-6 Unit cell dimensions for the three reported structures of $GdSi_x$ ($1.7 \leq x \leq 2$).

Crystal type	a	b	c	ref.
Tetragonal	4.10		13.61	83
Orthogonal	4.09 4.080	4.01 3.996	13.44 13.41	86 80
Hexagonal	3.877 3.864		4.172 4.155	87 80

Table 2-7 Anomalous densities for orthorhombic rare earth silicides.

Silicide	Density (ideal) [g/cm^3]	ref.	Density (meas.) [g/cm^3]	ref.
$DySi_2$	6.8	55	5.2	56
$GdSi_2$	6.4	55	5.94	86

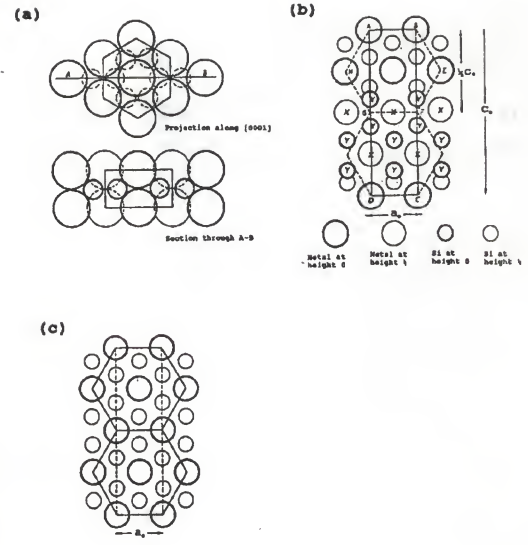

Figure 2-1 Hexagonal and tetragonal lattices for $ThSi_2$
(a) ß-$ThSi_2$ (hexagonal AlB_2-type) packing diagram.
(b) Tetragonal structure cell of α-$ThSi_2$ projected along [010] direction.
(c) Hexagonal structure cell of ß-$ThSi_2$ projected along [0001] direction.

CHAPTER THREE
DEPOSITION AND ANALYTICAL TECHNIQUES

Introduction

Ion-beam sputter deposition from a composite target of silicon and gadolinium was used to produce $GdSi_x$ films on Si, GaAs and amorphous quartz slides to study the properties of codeposited mixtures. For comparison, sample thin films of gadolinium disilicide were produced by thin film reaction of electron-beam deposited rare earth metal with substrate silicon or deposited amorphous silicon, but the times, temperature, and completion of the reaction were so unpredictable because of oxygen contamination that this approach was found impractical for producing silicides.

Compositions of the codeposited films were varied from N_{Si}/N_{Gd} of 14:1 to 1:1. These films were then studied in comparison to the thin film reaction product and to a bulk-prepared disilicide from Cerac, Inc.

The composition was evaluated using Rutherford backscattering spectroscopy (RBS) and Auger electron spectroscopy (AES).[89] The AES instrument used, having enhanced imaging and areal resolution capabilities, is also known as a scanning Auger electron microprobe (SAM).

Post-analysis using SAM showed that divergent RBS data resulted from topography in the reacted-film and heterogeneous phase formation in the bulk-prepared samples, respectively. AES spectra from the homogeneous regions of the two silicides was used to evaluate homogeneous Gd/Si films deposited from the composite sputter target.

Evaluation of surface composition gradients and the development of quantitative Auger electron spectroscopy for the Gd/Si system will be presented separately, in Chapters Four and Five.

The structure of the films were studied using x-ray diffraction (XRD)[89] and also electron diffraction in the transmission electron microscope (TEM). Other measurements obtained included the resistivity (by the four-point probe technique), optical properties (using optical absorption and reflectometry), and contact properties (using current-voltage measurements of 0.7mm-diameter dot contact diodes, deposited through a mechanical mask). These results are presented in Chapter Six.

Thin Film Deposition

All substrates were degreased using a standard cleaning procedure (TCE - Acetone - Methanol). Silicon and GaAs substrates were then chemically etched in a solution of 1:10 $HF:H_2O$ to remove surface oxides. Samples for ion-beam deposition were further cleaned under vacuum in the

deposition chamber by exposing the sample surface to a flux of ≈300eV Ar^+ ions before deposition.

Ion-beam sputter codeposition

The problems inherent in the thin film reaction approach provided incentive to develop a codeposition process in which the silicon and gadolinium are deposited as a stoichiometric mixture, thus avoiding both excessive oxidation of the metal before heat treatment and irregularities in the films due to uneven redistribution of species in the course of the reaction. Besides, the cosputtering technique was desirable in terms of demonstrating reasonable film qualities that could be transferred to applications without elaborate techniques that are time-consuming and expensive. Finally, the cosputtering approach was made more attractive by the development of a target configuration that allowed for tuning the Gd/Si ratio by altering the orientation of the composite target of Si and Gd [Figure 3-1]. Compositions of the films were varied from N_{Si}/N_{Gd} of 14:1 to 0.87:1, and by comparative analysis the deposition of films near the desired $GdSi_{1.7}$ composition was maintained. The codeposited films were free of the roughness and pitting typical of the reacted films.

The deposition chamber was a conventional VEECO Microetch system consisting of a diffusion-pumped glass bell jar, with a base pressure of ≈$1x10^{-6}$ Torr, backfilled with

$5x10^{-6}$ Torr of Ar during sputtering. The ion source produces a uniform parallel beam of ions with an accelerating voltage adjustable in the 0-3keV range, allowing substrate cleaning with lower-energy ions while depositions were done at 2keV. A quartz crystal thickness monitor mounted in the chamber was calibrated and cross-checked by profilometer measurements on the deposited films. Mechanical shadow masks fabricated from tantalum metal foil were used to define circular diode test patterns as required for contact measurements.

Silicides formed by reaction of deposited Gd metal

In order to assess the properties of silicides produced by the thin film reaction approach, thin films of Gd metal were prepared by electron beam evaporation and magnetron sputter deposition for reaction studies, both on silicon and GaAs substrates.

Films of Gd metal were deposited by electron beam evaporation in an ion-pumped chamber, with turbo-pumping to assist in handling the gas load during evaporation. The base pressure in the system was $\approx 1x10^{-6}$ Torr and the pressure during evaporation was $\approx 5x10^{-5}$ Torr.

Samples were coated to various thicknesses with Gd or Gd/Si layers. All samples were capped with ≈20nm of silicon to protect the surface from oxidation during sample transfer to analysis.

Additional samples of Gd on Si were prepared by DC magnetron sputter deposition in a diffusion-pumped chamber, base pressure $\approx 1 \times 10^{-6}$ Torr, backfilled with Ar gas during deposition. The substrates were chemically cleaned, and then plasma cleaned in the chamber. Again, they were capped with silicon (≈20nm) before removing them from the chamber.

The thin film reaction has several disadvantages as a technique for producing silicide films. The deposited rare earth metal films are extremely susceptible to oxidation[7,59] and the reaction has a tendency to produce an irregular and pitted interface with the silicon. Good results from the reaction require careful attention to the cleanliness of the substrate surface and annealing under vacuum or a strongly reducing atmosphere.

For measurement of some intrinsic properties and for applications to compound semiconductors, it is desirable to produce the silicide on substrates other than silicon. This would require alternate or multiple layers of Si and rare earth metal of appropriate thickness ratio with subsequent reaction to form the silicide. The reaction of deposited gadolinium with overlayers of amorphous silicon does offer advantages in that reaction has been shown to occur at lower temperatures and to produce smoother films than the reaction with crystalline substrates.

Some attempts were made to create reacted films on non-silicon substrates but were abandoned since the difficulty

of producing uniform films of correct stoichiometry using this approach was difficult, and optical analysis was a priority that required this uniformity. This approach requires the deposition of a bilayer (or multilayer) of Gd and Si in appropriate thickness ratio, or alternatively deposition of a surplus of Si as a cap for the annealing process (subsequently to be removed).

However, the technique is unattractive in terms of controlling processing parameters. That is, while such multilayer structures have the potential for reducing or eliminating the pitting and unevenness of the films, and could produce silicide films on substrates other than silicon, considerable complications are introduced in controlling the deposition and reaction.

Analytical Instruments

RBS.[89] The samples were analyzed using 2.0 MeV alpha particles with a beam current of 120 nAmp. Spectra were smoothed and stoichiometries determined by fitting with self-consistent stopping-power calculations. The chamber was equipped with a resistive heating stage and reaction of thin films of Gd on Si substrates was monitored in situ.

SAM.[89] The AES data were acquired on a PHI 660 Scanning Auger Microprobe in the N(E) mode. Base pressure in the analytical chamber was $\approx 4 \times 10^{-10}$ Torr, with primary beam energy of 10keV and a beam current ≈400 nAmp. The surfaces

were sputter-cleaned using a differentially pumped ion gun. Chamber pressures during sputtering were $\approx 8 \times 10^{-8}$ Torr. The areal resolution and imaging capabilities of the SAM made it very useful in comparing the silicides prepared by the various techniques.

XRD.[89] Measurements were carried out with a Phillips powder diffractometer using Cu K_α radiation and the crystallization properties of the films were studied using a hot-stage sample holder.

Composition of Films

The reacted thin film specimens along with bulk-prepared $GdSi_2$ provided a reference for comparison with the codeposited Gd-Si films. Relative heights of the leading edges of the Si and Gd elemental transitions in the RBS spectra was used as an alternative method for determining the compositions [Figure 3-2]. Peak height ratios (Gd/Si) and integral peak areas were not entirely consistent among the three types of samples.

Subsequent examination of microstructure in the bulk disilicide by SAM showed platelets of a silicon-rich precipitate which has been identified as silicon carbide. The presence of this second phase is believed to result from reacting a silicon-rich 2:1 Si:Gd mixture in a graphite crucible, while the stable silicide is $GdSi_{1.7}$.[80] When the matrix phase of the bulk disilicide was analyzed (as

compared to the excess silicon phase in the granules) by SAM, it compared favorably with the fully reacted thin film silicides and with films of 1.7:1 (RBS) stoichiometry deposited by sputtering.

It was also noted that samples produced by thin film reaction exhibited a very rough surface and pitted interface with the substrate. Neither of these fit the RBS model of a planar layerwise-homogeneous sample. The codeposited films, which physically resemble the RBS model, were evaluated for uniformity, and compositions were calculated from the RBS model.

Thus multiple phases and topography effects were found to cause disagreement between the SAM and RBS for the bulk silicide and the reacted films. For the smooth homogenous films deposited by the ion beam technique, RBS and SAM stoichiometry data can be compared directly and showed good agreement after application of matrix-corrected AES sensitivity factors, which are developed in Chapter Seven. The corrected AES measurements facilitated the monitoring of composition in subsequent depositions.

The polymorphism of the rare earth disilicides mentioned above has some significance to the questions of composition and structural analysis for these films, and will be discussed below in Chapter Six.

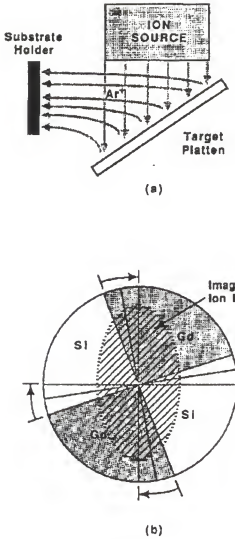

Figure 3-1 Codeposition from a composite sputter target.
(a) Profile view of diode ion-beam sputter apparatus.
(b) Face-on view of the target, showing the image of the ion beam on the target, with composition of the sputtered flux controlled by rotation of the target.

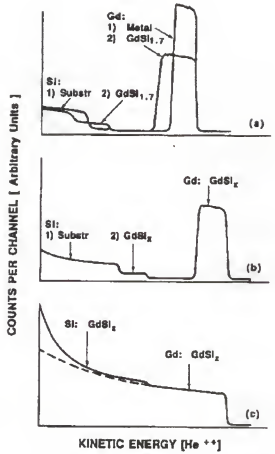

Figure 3-2 RBS analysis of gadolinium disilicides.
(a) Thin film reaction: 1) RBS spectrum of a Gd metal film as deposited on a Si substrate, and 2) after reaction (T=400°C). In formation of the silicide, the silicon peak has shifted to the surface with a lower peak height; the gadolinium peak is reduced in height and broadened.
(b) Codeposited Gd-Si mixture: stoichiometry is determined by comparing the integral counts in the silicon shoulder and in the Gd peak. These samples provide the most accurate results because they more closely conform to the RBS model of planar, layerwise homogeneous samples.
(c) Bulk-prepared disilicide: comparison of peak heights of the leading edges of the Gd and Si transitions can be compared with the thin film specimens.

CHAPTER FOUR
ANGLE-RESOLVED X-RAY PHOTOELECTRON SPECTROSCOPY (ARXPS)

Introduction

Formation of contacts by vacuum deposition requires an understanding of the condition of surfaces. Chemically cleaned substrates quickly develop an oxidized surface layer in the ambient. Sputter cleaning can change the surface composition of a compound semiconductor substrate and preferential sputtering affects the results of film analysis as well.

Electron spectroscopies produce compositional data by measuring the relative intensities of photoelectrons or Auger electrons emitted by a sample under an excitation beam of high energy photons or electrons. The signal electrons counted are those that escape the sample without significant loss of energy from their characteristic excitation peak. The depth analyzed is thus related to the inelastic mean free path, that is the average distance traveled without an energy-loss scattering event.

Angle-Resolved X-ray Photoelectron Spectroscopy (ARXPS) has been recognized as a potential method for non-destructive determination of a composition depth profile of a surface region that is dimensionally comparable to the

mean free path of the photoelectrons. Typical values for the mean free path are on the order of 10 to 50 Å. The ability to resolve composition changes within so narrow a surface region combined with the non-destructive nature of the analysis makes the technique particularly attractive for studies of thin films, interfaces, and surfaces.

An inverse Laplace transform method has been used to extract composition depth profiles from angle-resolved x-ray photoelectron spectroscopy (ARXPS) data from oxidized Si and Ar^+ bombarded GaAs. An iterative procedure determines a least-squares curve-fit of the data using the Laplace transforms of step functions, which are summed to yield the composition profiles.

In this chapter, after introducing the model and the iterative approach developed, which gives a self-consistent solution to the flux equation, two example applications are presented. 1) A sample of native oxide is present on a Si wafer, for which the composition profile derived defines the thickness and chemical layering of the various silicon oxide states, and 2) samples of GaAs have been sputtered with 1.5, 3.0, and 5.0 keV Ar^+, where the composition depth profiles show a subsurface As depletion the extent of which increases with increasing ion energy, resulting from preferential sputtering caused by surface segregation enhanced by sputter-assisted diffusion in the near surface region.

The Inverse Laplace Transform: An Iterative Solution

A simplified expression of the photoelectron flux generation and attenuation in the sample has been shown to take the form of a Laplace transform of the depth composition function.[90] Unfortunately, the inverse Laplace transform relation does not define a unique solution, but rather an extensive and varied set of solution functions whose transforms are nearly identical.[91] Consequently the numerical solution of the composition function has required elaborate computational techniques combined with constraints on the form and the range of the solution function.

A new approach to the problem has been introduced in which the ARXPS data are curve-fitted using the concisely defined Laplace transforms of simple step functions.[92] Iterative error reduction by least-squares comparison yields a solution consisting of summed step functions as an approximation of the composition function. This procedure does not involve restrictions on the form of the solution and reduces considerably the complexity of the computations involved. In this work, the data reduction technique has been applied to ARXPS data from two different types of single crystal semiconductor substrates with altered surface layers. First, the thin native oxide on a (100) Si substrate was analyzed using the Si 2p photoelectron peaks of the XPS spectrum. In addition to the core line representing the elemental Si substrate, several shifted peaks were resolved

with binding energies identified with distinct oxidation states of the silicon (i.e., SiO, Si_2O_3, and SiO_2). The location and relative abundance of Si in each of these oxidation states was recovered from the ARXPS data. The second example is (100) p-type GaAs ($5x10^{18}$ cm^{-3} Zn) analyzed after 1.5, 3.0, and 5.0 keV Ar^+ ion etching. Changes in surface and subsurface composition produced by the ion bombardment are discussed in the context of preferential sputtering.

The ARXPS Flux Model

XPS is a surface sensitive analytical technique because of the rapid energy attenuation of low energy electrons in a solid. This surface sensitivity can be increased by changing the take-off direction for electrons entering the analyzer toward grazing angles relative to the sample surface [Figure 4-1]. This decreases the effective escape depth of the photoelectrons, quenching the signal arising from deeper layers of the sample, thus yielding collected data that are enriched in surface information.

The intensity of photoelectron flux from a given element with a concentration $C_i(x)$ is a function of the angle θ, given as[93]

$$I_i(\theta) = K_i(\theta)\,\sigma_i \int_0^{\infty} C_i(x)\, \exp\left(\frac{-x}{\lambda_i \sin\theta}\right) dx \qquad (4\text{-}1)$$

For a given photoelectron energy, $K_i(\theta)$ represents a combination of the effective analyzer response function and the excitation flux as a function of θ. The product of this excitation flux, the depth composition function $C_i(x)$, and the photoionization cross-section σ_i, is a generation factor. The exponential term represents the attenuation of the flux contribution from a depth x analyzed at the angle θ.

Normalizing the intensity with respect to $K_i(\theta)$ and σ_i

$$\overline{I_i}(\theta) = \frac{I_i(\theta)}{K_i(\theta)\,\sigma_i} = \int_0^\infty C_i(x)\,\exp\left(\frac{-x}{\lambda_i \sin\theta}\right) dx \qquad (4\text{-}2)$$

and comparing equation (4-2) with the Laplace transform of a function f(x),

$$L[f(x)] = \int_0^\infty f(x)\, e^{-px} dx = F(p) \qquad (4\text{-}3)$$

it is clear that, within the assumptions of the model, the normalized XPS intensity as a function of take-off angle is a Laplace transform of the composition depth profile (CDP) of the specimen, with $p = 1 / \lambda \sin(\theta)$ as the parameter of the exponential term.

Several studies have made use of this model of the generation and attenuation of the photoelectron flux to extract quantitative information concerning inhomogeneities in the CDP. For the most part the samples have been modeled as a homogeneous substrate having an abrupt interface with a single homogeneous overlayer.[94-98] These single overlayer

models have limited applicability in surface science. It has recently been demonstrated that reconstruction of non-monotonic CDPs (i.e. profiles with both positive and negative gradients) is achievable by layer-wise iterative solution by curve-fitting using Laplace transforms.[92] The fitting curves are thus self-consistent with the exponential flux attenuation model. However, it must be born in mind that a unique solution with good quantitative agreement between depletion/accretion depths, magnitudes, and gradients cannot be uniquely and accurately determined from ARXPS data.[92]

The model flux equation assumes an atomically smooth sample surface, and negligible dispersion effects on both photon and photoelectron fluxes.[99] The single crystal substrates analyzed in the present work exhibit minimal surface roughness, while the altered surface layers are expected to have an amorphized structure that will wash out the diffraction peaks or forward-scattering effects observed in angle-resolved photoemission from single crystals.[100]

Example 1: Oxidized Silicon

The Si samples were analyzed in a Perkin-Elmer PE5950 XPS spectrometer. This instrument provides high angular resolution and high count rates even at very low grazing angles. The resulting uniform angular response permits data collection across a wide range of sample tilt angles [Figure

4-2]. The spectrometer was operated at a resolution of 0.01 eV full width at half maximum (FWHM), and at a pressure of less than 10^{-8} Torr. The Si wafers were chemically cleaned, then oxidized (in the ambient atmosphere). The samples were characterized using a 0 to 1000 eV wide scan for elemental analysis followed by examination of the Si 2p lineshape.

The XPS spectra of the Si 2p region was recorded at takeoff angles of 10°, 30°, 60°, and 90°. After background correction the peaks were curve-fitted using a PHI software program. In addition to the Si 2p doublet associated with the elemental substrate, shifted peaks associated with SiO, Si_2O_3, and SiO_2 bonding were resolved [Figure 4-3, Table 4-1]. The doublet structure was not resolved in the shifted peaks. The resolved peaks were integrated and normalized to the total Si 2p peak at each angle, resulting in a plot of fractional flux versus take-off angle for each suboxide [Figure 4-4]. These data were then solved for the depth distribution of each oxidation state independently, without imposition of a mass balance constraint.

The solutions [Figure 4-5] show the SiO_2 as the principle constituent of the oxide overlayer with the SiO and the Si_2O_3 at the SiO_2/Si interface in the expected sequence of decreasing oxidation with depth. The composite of these separate solutions comes close to unit composition despite the lack of an explicit mass balance constraint. The relative intensities of the all three surface oxide peaks as

measured at the normal take-off angle fall below the expected values, while the elemental Si signal is stronger. This is understandable as the effect of the strong forward-scattering peak expected from the substrate along the (100) crystallographic direction, that is, the surface normal.[96]

The solutions for the CDP's are plotted as functions of relative depth x/λ, where λ is the mean free path (MFP) of the Si 2p photoelectrons. The value of λ is material-dependent; it can be taken as $\approx 27 \pm 6$ Å in the Si substrate, and is expected to increase to $\approx 37 \pm 4$ Å in the oxide layer.[96] Since there is considerable uncertainty in these values, a constant λ is used in these plots with the understanding that the effects of (1) lower number density of silicon atoms and (2) longer electron MFP expected in the oxide layer will act in opposition in the flux equation. In essence it is hoped that the terms cancel out in plotting the depth profile using a constant value for the MFP.

Example 2: Sputter Altered Surfaces of (100) GaAs

The GaAs samples were analyzed in a Kratos XSAM-800 spectrometer. The wafers were cleaned using a 4:1:1 mixture of H_2SO_4:H_2O_2:H_2O. They were then Ar^+ sputtered using a differentially pumped ion gun with a rastering beam incident at 20° relative to the sample surface. During the sputtering the system pressure was held at 10^{-9} Torr. A steady-state

was reached at each of the ion energies (1.5, 3.0 and 5.0 keV) as determined by monitoring of the time transients in the As 3d and the Ga 3d regions.

ARXPS spectra from the GaAs were taken at takeoff angles from 10° to 90° at 10° intervals. The composition profiles derived [Figure 4-6] show a surface composition near the bulk value, a subsurface depletion of As, then a return to the bulk composition at greater depth. The subsurface depleted region occurs at increasing depth with increasing ion energy. The MFP of the sputter-altered region has been assumed equal to the MFP of the bulk.

A review by Kelly[101] described a sputter-induced profile similar to these, with a subsurface depleted region and a surface near the bulk composition, as the expected steady-state for an alloy exhibiting bombardment-induced Gibbsian segregation.

Gibbsian segregation arises from a standard thermodynamic treatment of a regular solution alloy, having an arbitrary heat of mixing, ΔH_m, but an ideal entropy of mixing. If there is an enthalpy change associated with the exchange of an A atom on the surface with a B atom in the bulk, then the steady-state surface composition will be[101]

$$\frac{C_{A(s)}}{C_{B(s)}} = \frac{C_{A(b)}}{C_{B(b)}} \exp\left(-\frac{Q}{RT}\right) \qquad (4-4)$$

where Q is the heat of segregation, with $C_{i(s)}$ as the surface concentration and $C_{i(b)}$ as the bulk concentration of

component i. The enthalpy term, Q, may be attributable to both chemical binding and strain effects.

Under conditions of steady-state sputtering, the surface composition is evaluated from the conservation relation,

$$\frac{C_{A(s)}}{C_{B(s)}}\frac{Y_A}{Y_B} = \frac{C_{A(s)}}{C_{B(s)}}Y_{AB} = \frac{C_{A(b)}}{C_{B(b)}} \qquad (4\text{-}5)$$

where Y_i is the sputter yield for ions impinging on the component i in the target and Y_{AB} is a ratio taking into account preferential effects such as energy transfer or chemical binding.[101]

In Gibbsian segregation the surface composition $C_{i(s)}$ is related to the subsurface composition $C_{i(2)}$ according to equation (4-6), that is,

$$\frac{C_{A(s)}}{C_{B(s)}} = \frac{C_{A(2)}}{C_{B(2)}}\exp(-\frac{Q}{RT}) \qquad (4\text{-}6)$$

Thus during sputtering the subsurface layer will be depleted of the component which segregates. For ion-bombarded specimens, diffusion in the undamaged bulk region is expected to be slow compared to the sputter removal rate. A very steep concentration gradient will result, with mass transport largely confined to the ion damage region where the high defect density will lead to enhanced diffusion rates.

This mechanism for the observed preferential sputtering and the resulting composition profile help to explain the conflicting results in preferential sputtering of different systems (e.g. CuAu alloys) when AES vs. ISS has been used to study the phenomenon.[102] Analysis by XPS or AES with the analyzer at a fixed takeoff angle to the sample surface will indicate a depletion of the surface-segregating species due to the predominance of the depleted region in the analyzed volume, while analysis by ISS will show the topmost layer to have approximately the bulk composition.

The GaAs profiles derived from ARXPS support this model for preferential sputtering effects. The increasing extent of the depleted region with increasing ion energy suggests that this disturbed layer is coincident with the penetration range of the bombarding ions for these energies.

Conclusion

ARXPS has been demonstrated as a practical technique for non-destructive depth profiling of an extremely narrow surface region of suitable samples. In the case of the oxidized Si samples, the location and relative abundance of Si in each of these oxidation states was recovered from the ARXPS data. The sputtered GaAs composition profiles show a surface composition near the bulk ratio, a subsurface As depletion, then a return to the bulk composition at greater depth. This supports the mechanism of preferential

sputtering due to Gibbsian surface segregation, the As on the surface being replenished by diffusion from the disturbed layer with a diffusion rate enhanced by the high defect density in the bombarded region.

The application of these results to this study gives a more detailed understanding of the surface oxide of an air-exposed silicon substrate, for example. While this contamination layer may be readily sputtered away before deposition of the silicide, for GaAs sputter-cleaning means the silicide will be deposited on a non-stoichiometric surface. This can be expected to have an influence on the interface formation and contact properties, as will be discussed in Chapter Six.

Sputter-induced changes in surface composition also adds a complication to routine surface analysis of compounds such as the silicide films, since sputter cleaning and sputter-depth profiling are commonly used in Auger electron spectroscopy as well as XPS. The alteration of surface composition in the sample, along with a number of other factors, must be considered in a full treatment of AES data, to be taken up next in Chapter Five.

Table 4-1 Binding energy separation [in eV] of the peaks deconvoluted from the Si 2p XPS region as shown in Figure 4-3. The elemental 2p 3/2 peak is used as a reference.

	Binding energy separation [in eV] measured from Si 2p 3/2 (elemental)			
Angle	Elem. Si 2p 1/2	Si^{2+}	Si^{3+}	Si^{4+}
90°	0.67	1.77	2.67	4.17
30°	0.67	1.77	2.67	4.17
20°	0.67	1.77	2.47	4.17
10°	0.63	1.83	2.73	4.23

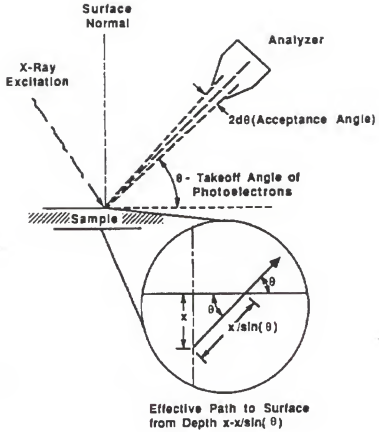

Figure 4-1 The geometry of the analyzer. The signal recorded is constrained to the takeoff angle θ, and the effective path to the surface for flux from a point x below the sample surface becomes $x/\sin(\theta)$.

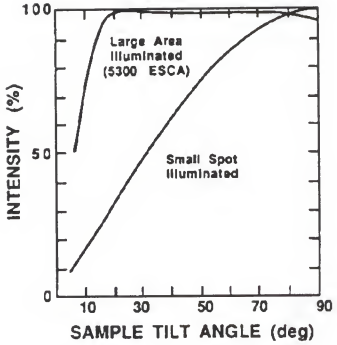

Figure 4-2 Plot of signal intensity versus sample tilt angle for the Perkin Elmer PE5950 ESCA

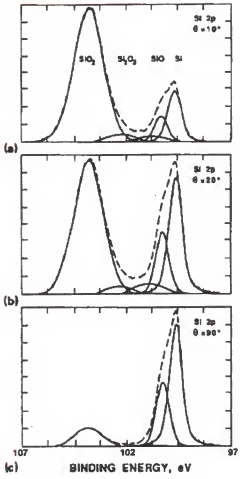

Figure 4-3 Silicon 2p spectra from a silicon wafer with a native oxide layer, at three sample tilt angles. The raw spectrum has been Gaussian curve-fitted with five components to the fit: the Si 2p elemental peak (doublet), along with three shifted peaks associated with the SiO_2, SiO and Si_2O_3 oxidation states.

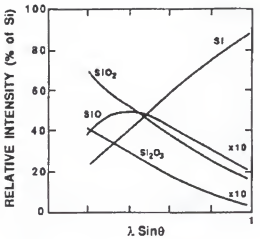

Figure 4-4 Plot of relative silicon species intensities versus analysis depth $\lambda\sin(\theta)$, where θ is the sample tilt angle.

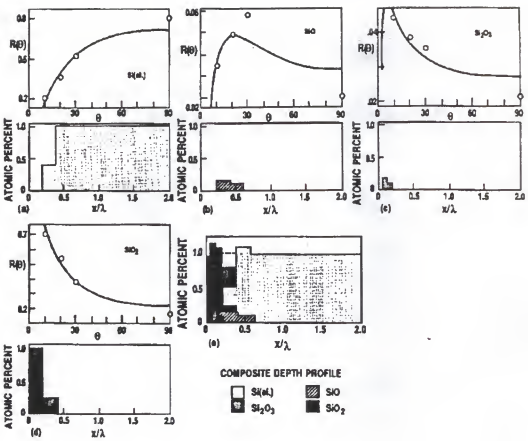

Figure 4-5 ARXPS results for the oxidized silicon wafers, with relative intensity measurements [data points $R(\theta) = I(SiO_x)/I(Si_{TOT})$] for each of the components of the Si 2p region of the XPS spectrum, plotted versus takeoff-angle θ (see Figure 6-3). Curve-fit [____] represents the Laplace transform of the step-function CDP depicted. The atomic percent plotted is actually the relative percentage of Si in each oxidation state, ignoring other species present (such as oxygen). (a) elemental Si, (b) SiO, (c) Si_2O_3, (d) SiO_2, (e) a composite of the CDPs for all subspecies. The solution profiles are consistent with a layered structure of sub-oxides at the interface. The solutions were derived independently, without constraint to yield 100% as the total composition.

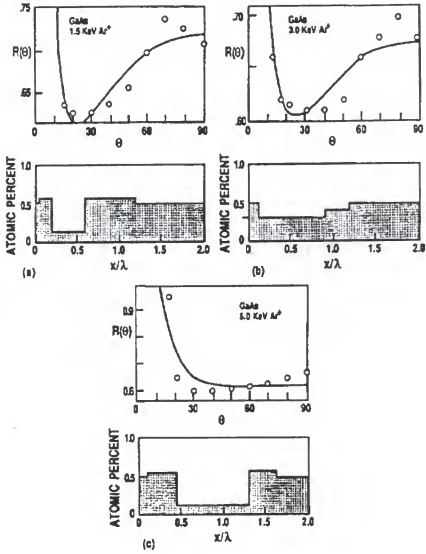

Figure 4-6 ARXPS results for the Ar^+ sputtered GaAs, using the Ga 3d and As 3d XPS peaks. Relative As intensity ($I_{As}/(I_{As}+I_{Ga})$) is plotted as data points R(θ) , with curve-fit [_____] using the Laplace transform of the step-function CDP depicted (atomic percent As vs. relative depth, x/g): for Ar^+ ion energies of (a) 1.5 keV, (b) 3.0 keV, (c) 5.0 keV. Note the region of subsurface As depletion, and the progression of the depleted region to greater depth with increasing ion energy.

CHAPTER FIVE
QUANTITATIVE AUGER ELECTRON SPECTROSCOPY IN THE Gd-Si SYSTEM

Introduction

Quantification of Auger electron spectra from rare earth silicides requires correction of the elemental sensitivity factors due to matrix effects. In this analysis the Si KLL, Si LVV, Gd MNN, and Gd NNN/NVV Auger transitions have been measured for a number of samples. Composition was calculated using the data from the higher kinetic energy regions (Si KLL and Gd MNN). Comparison of Auger data with RBS results yielded composition-dependent effective AES sensitivity factors, S^{eff}, using the RBS stoichiometries of the codeposited films as the necessary reference bulk analysis.

In addition, several qualitative or semi-quantitative observations are made including (1) rates of oxygen uptake by sputter-cleaned surfaces and consequent changes in the AES lineshape, (2) changes in AES lineshape in the Si KLL region attributable to silicide formation, (3) loss features in the elastically backscattered primary beam and comparison with the backscatter from elemental samples of the constituents.

Experimental

Samples analyzed included thin films of disilicide formed by reaction of Gd metal films on Si substrates and co-sputter-deposited Gd-Si mixtures. In order to confirm the compositions, a sample of bulk-prepared disilicide was polished for use as a standard in the analyses. Details concerning the RBS and AES instrumentation have been covered in Chapter Three.

The RBS analysis of the reacted thin films was consistent with the reported single-phase $GdSi_{1.7}$ reaction product, but the reaction produces a pitted surface and a nonplanar interface with the substrate, reducing the level of confidence in the stoichiometric values derived from the RBS. The disilicide standard on the other hand had inclusions identified as SiC. In view of the SiC inclusions in the bulk disilicide and the roughness of the reacted-thin-film interface, it was apparent that the only reliable calculated RBS stoichiometries were those for the codeposited films.

AES composition values were derived from the data using peak-to-peak measurements in the dN(E)/dE mode after numerical differentiation. The dN(E)/dE measurements are strongly affected by the modulation voltage applied to the analyzer[103] (or equivalently the differential interval applied to the N(E) data). In this work, a differential

interval equivalent to a 4 volt peak-to-peak modulation voltage was used in the differentiation.

The RBS compositions of the codeposited films were found to fall in a range of Si:Gd = 1.0 to 14.0. Since the composition of the freely-formed reaction product was regarded as desirable in terms of stability, and given the difficulty in comparing the RBS results among the three types of samples, it was necessary to develop a capability to assess the composition of the codeposited films in comparison with regions of fully reacted thin film samples and the precipitate-free matrix of the bulk disilicide.

Thus the problem was defined as determining the AES fingerprint of the $GdSi_{1.7}$ disilicide phase, and assessing the effect of composition and contamination on AES measurements in the Gd-Si system.

Quantitative AES

The quantification of Auger electron data begins with an expression for the Auger electron current, $I_i(UVW)$ (hereafter $I_i(X_i)$), from the UVW Auger transition of the i^{th} element[104]

$$I_i^{UVW} = I_p \cdot \Gamma_{UVW} \cdot \phi_i^{(E_p, E_U)} \cdot C_i^{(E_p, E_U)} \cdot R \cdot T \cdot N(X_i^s) \cdot \lambda(X_i^s) \cdot r_i^{(E_p, X_i^s)} \cdot X_i^s \qquad (5\text{-}1)$$

where I_p= primary current, $\Gamma(UVW)$ = Auger transition probability, $\phi_i(E_p, E_u)$ = ionization cross section of the U level which is a function of the primary energy E_p and the

critical energy for U level ionization E_u, $C_i(E_p,E_u)$ = the Auger and Coster-Kronig contributions to electron holes in the U level, R = surface roughness factor, T = instrument response function, N = atomic density, λ = electron inelastic mean free path (IMFP), r_i = electron backscatter coefficient, and X_i^s = atomic fraction of the i^{th} component in the volume detected at the surface.

The factors Γ, T, ϕ_i, and C_i are matrix insensitive. The matrix sensitive factors N, λ and r are functions of concentration. I_p is subject to instrumental control, within the restrictions on its accurate measurement. R may vary from sample to sample depending upon initial topography and sputter-induced changes in topography. Lastly, the surface composition X_i^s may differ from the bulk due to surface segregation especially under the ion bombardment that is commonly used to prepare a clean surface for analysis.

Quantification of data from AES can be attempted using one of three approaches:[105]

1. First-principles approach: evaluation of terms in the Auger current equation.
2. Elemental standards: correcting only for matrix effects.
3. Use of a series of standards with a composition near that of the unknown.

The first two have the great advantage in that, if successful, they implicitly have the potential for allowing

samples of arbitrary composition to be quantitatively analyzed. However, in actuality the evaluation of the terms describing both matrix-insensitive and matrix-sensitive terms is dependent upon empirical fitting of experimental measurements, with significant scatter in the fits and a resulting large margin of error in the evaluations.[105] On the other hand, the use of standards minimizes or eliminates the effects of many factors in the AES flux equation. In addition, by comparison of results from AES with results from a more quantitative technique and using sensitivity values from elemental standards, one can derive a single correction term S_i^{eff} for matrix M that will bring all of the results into agreement.

This can be expressed as follows: for a pure elemental sample, an elemental sensitivity factor S_i^o can be defined[106,107] as

$$S_i^o = \frac{I_i^o}{I_p} \qquad (5\text{-}2)$$

where I_i^o is the Auger current from a pure sample of element i and I_p is the primary beam current.

For a pure elemental sample there can be no segregation effects, so $X^s_i = X_i$. Therefore from Eqs.(5-1) and (5-2),

$$S_i^o = \Gamma_{UVW} \cdot \Phi_i^{(E_p, E_0)} \cdot C_i^{(E_p, E_0)} \cdot R \cdot T \cdot N_i^o \cdot \lambda_i^o \cdot \sigma_i^o(E_p) \ . \qquad (5\text{-}3)$$

From this expression can be derived the relative elemental sensitivities S_i^{rel} as tabulated in the Handbook of Auger Electron Spectroscopy[108]

$$S_i^{rel} = \frac{S_i^o}{S_s^o} \tag{5-4a}$$

$$= \frac{I_i^o}{I_s^o} \tag{5-4b}$$

$$= \frac{G_i}{G_s} \cdot \frac{T_i}{T_s} \cdot \frac{N_i^o \cdot \lambda_i^o \cdot r_i^o(E_p)}{N_s^o \cdot \lambda_s^o \cdot r_s^o(E_p)} \tag{5-4c}$$

where the subscript S refers to a standard reference peak in a pure elemental sample (typically the Ag 351 eV peak). The matrix-insensitive factors relating to ionization and transition probabilities have been condensed into the terms G_i and G_s, and differences in surface roughness are ignored.

Presuming that the natural shape of a given feature is described by G_i, and that the analyzer and detector response during the acquisition (including modulation voltage or numerical differentiation window for dN(E)/dE measurements) is the same as that for the elements, correct measurements then depend upon evaluation of the terms involving the matrix-dependent factors N, λ and r. Thus all the elemental parameters are normalized in a self-consistent fashion, with the caution that the transmission of the analyzer and detector response may vary greatly under various operating conditions of the same instrument.

Matrix-Corrected Sensitivity Factor S^{eff}

Relative elemental sensitivities can in many cases be evaluated directly by comparison of measured intensities from prepared standards (Eq.(5-4b)), without evaluating the separate terms of Eq.(5-4c). However, for evaluating the composition of arbitrary samples a more general approach is desired.

To parallel the notation used for the matrix terms by Mathieu and Landolt,[109] a corrected sensitivity factor S_i^{eff} for the elemental ransition i in matrix M can be expressed as the product of the elemental sensitivity S_i^o and a matrix correction factor k^M_i:

$$S_i^{eff} = k_i^M \cdot S_i^o \tag{5-5}$$

where

$$k_i^M = k_i^N \cdot k_i^\lambda \cdot k_i^r \cdot k_i^s \cdot k_i^T \tag{5-6a}$$

and

$$k_i^N = \frac{N_i^M}{N_i^o} \tag{5-6b}$$

$$k_i^\lambda = \frac{\lambda_i^M}{\lambda_i^o} \tag{5-6c}$$

$$k_i^r = \frac{r_i^M}{r_i^o} \tag{5-6d}$$

$$k_i^s = \frac{X_i^s}{X_i^M} \tag{5-6e}$$

$$k_i^T = \frac{T_i^M}{T_i^o} \; . \tag{5-6f}$$

The superscript ^{M} refers to values pertaining to the given matrix; the superscript $^{\circ}$ refers to the elemental matrix i.

Combining Eqs.(5-1)-(5-3) and Eq.(5-5) gives the intensity from element i in matrix M,

$$I_i^M = I_p \cdot k_i^M \cdot S_i^\circ \cdot X_i \tag{5-7}$$

and the atomic fraction of element i,

$$X_i = \frac{I_i^M}{I_p \cdot k_i^M \cdot S_i^\circ} \tag{5-8a}$$

$$= \frac{I_i^M}{I_s^\circ \cdot k_i^M \cdot S_i^{rel}} \ . \tag{5-8b}$$

For comparison of peaks i and j of two elements in the matrix M,

$$\frac{X_i}{X_j} = \frac{k_j^M}{k_i^M} \cdot \frac{S_j^\circ}{S_i^\circ} \cdot \frac{I_i^M}{I_j^M} \ . \tag{5-9}$$

Evaluation of matrix-dependent terms

Attempts have been made[110-115] to evaluate the matrix-dependent terms in Eq.(1) which bear directly on the terms k_i^N, k_i^λ, and k_i^r, describing the number density of atoms, the electron mean free path, and backscatter of the primary electron beam. Hall and Morabito[110] evaluated the matrix-dependent parameters in detail, with a focus on dilute alloys.

(The terms corresponding to segregation and analyzer transmission, k_i^s and k_i^T, are not dealt with in these

treatments, but as noted they can have a serious impact upon results).

For the backscatter term, Hall and Morabito[110] relied upon an empirical equation given by Reuter,[111] designed for use with the electron microprobe:

$$r_I^M = 1 + 2.8\,(1-0.9\,E_c/E_p)\,\Omega', \qquad (5\text{-}10)$$

where E_c is the critical ionization energy of the initial core hole and Ω' is the matrix-dependent "backscatter coefficient", given for pure elements by

$$\Omega' = -0.0254 + 0.016\,Z - 0.000186\,Z^2 + 8.3\times10^{-7}\,Z^3 \qquad (5\text{-}11)$$

where Z is the atomic number of the matrix element.

On the other hand, Prutton and El Gomati[112] have suggested that the backscatter factor is linear in atomic number, based upon analysis of spectral backgrounds. The straight line fit given is

$$r = 1 + 0.15 + 0.152\,Z\,. \qquad (5\text{-}12)$$

For the inelastic mean free path λ, Hall and Morabito[110] considered both the results of Penn[113] and those of Seah and Dench.[114] While for a given element the results derived from these two approaches may be in considerable disagreement, in general the values are similar.

There is an advantage in using the formula for λ from Seah and Dench,

$$\lambda = A\cdot N^{-1/3}\cdot E^{-2} + B\,(E/N)^{1/2}, \qquad (5\text{-}13)$$

which for higher energies reduces to the second term. Then

with Eq.(5-6c) above k_i^{λ} can be approximated as

$$k_i^{\lambda} = (N_i^{o}/N_i^{M})^{1/2} \quad . \tag{5-14}$$

Number density in an unknown sample may be estimated, or else approximated by weighting the elemental densities according to fractional composition.

In this work, a modified version of the Reuter term was used in which calculated elemental backscatter values were weighted according to the sample's fractional composition. Comparable results were obtained using a simpler expression from Prutton and El Gomati,[112] which will be used below.

The term for number density was estimated by a weighted average of the atomic number density of the silicide and the elemental density of the element that is in excess, assuming formation of silicide is maximized. These values were found to be consistent with measured values for density as determined by calculations based on profilometry measurements of film thickness combined with measured mass gain on a crystal thickness monitor.

Combining (1) an evaluation of k_i^{N}, (2) an expression for k_i^{λ}, also in terms of number density (Eq.(5-14)), and (3) evaluating k_i^{r} using Eq.(5-12) with Z_M as the average Z for the matrix, gives an evaluation of the matrix correction factor

$$k_i^{M} = k' \cdot \frac{(1.15 + 0.0152\, Z_M)}{(1.15 + 0.0152\, Z_i^{o})} \cdot (N_M/N_i^{o})^{1/2} \tag{5-15}$$

where k' is introduced as a term to accommodate errors due to the approximations and other factors, such as possible surface segregation effects. It is emphasized once again that the factor for analyzer transmission, k_i^T (Eqs.(5-6a), (5-6f)) can lead to significant variations in measured intensity, given the warnings by Powell[115] et al. concerning variations in Auger spectra between laboratories. It is apparent that variations in the operating conditions even on the same instrument may have significant impact on results as well. In the present work this was dealt with explicitly by taking measurements from elemental standards including comparison with the Ag 351 eV peak before applying the above correction term, and thus k_i^T is treated as unity.

The value of this approach is twofold. It allows the immediate development and employment of quantitative AES analysis of samples within the range of certainty of the standards, with results that represent the greatest degree of accuracy currently obtainable from AES. The advantages of AES in rapid data acquisition, good detection limits, relatively uniform elemental response, and lateral resolution combined with reasonably accurate quantification can then be employed to great advantage in an ongoing study, without the need for repetitive compositional analyses by the more expensive and time-consuming quantitative techniques.

Secondly, after applying the correction term as a function of composition it is reasonable to discuss which factors in the Auger current equation would serve as reasonable explanations for any residual disagreement between AES and bulk analysis (as expressed by k' in Eq.(5-15)). While reasonable values for number densities may be available, there remains considerable uncertainty in the evaluations of λ and the backscatter r. In particular, the assessment of r ignores the differences to be expected in the susceptibility of peaks having different initial hole ionization energies, with respect to a backscatter excitation flux that would be expected to vary considerably as a function of energy. Assessments of this nature will ultimately serve to increase our knowledge of the first principles involved, and thus bring us closer to the realization of quantifiable AES of arbitrary unknown samples using the first-principles approach.

In summary, the strategy is now defined as evaluation of composition using simple corrections to elemental sensitivity factors which have been corrected for the response of the instrument. Comparison of these results with RBS results give values of k' that allow us to assess the accuracy of the model-derived parameters for N, λ and r. It is then feasible to discuss other possible factors in the AES data analysis, for instance sputter-induced surface composition changes as reported by Wirth et al.[116] in quantitative AES analysis of refractory metal silicides.

Results and Discussion

Qualitative Results

Elastic peak and backscatter

The elastically backscattered primary beam and its background was studied for several elemental samples and the silicides by lowering the energy E_p of the primary beam to 2.8 keV, to fall within the limits of the detector [Figure 5-1(a)]. The intensity of the elastically-scattered primary beam along with the background level at lower energies in these spectra provide a qualitative measure of the backscatter factor, and also indicate characteristic loss peaks for each material. The oxidized surface of the silicide exhibits a strong loss feature at ≈30 eV below the elastic peak, and significant reduction of the elastic peak height compared to the clean silicide surface. As the oxide was removed by ion sputtering, the loss peak at 30 eV decayed, while two new loss peaks appeared at ≈12 eV and ≈27 eV [Figure 5-1(b)].

Low energy region

In the interval of 0-160 eV occur the Si LVV and Gd NNN/NVV Auger lines. Because of the higher surface sensitivity due to the short IMFP for lower energy electrons and a nonlinear response of the detection system in this energy regime, these peaks are not optimal for purposes of quantification. The well-known chemical shift in the Si LVV

peak associated with oxide formation is also a negative factor in this regard [Figure 5-2], but the observed change in lineshape does serve as a useful monitor of oxygen incorporation in the silicides and oxygen uptake from the residual gas in the chamber. Changes in the 112-127 eV portion of the Gd lineshape were also observed on the oxidized surface, with the 112 eV and the 127 eV peaks decaying along with the appearance of a peak at 122 eV. The 138 eV Gd NVV peak is not noticeably affected by this oxidation [see Figure 5-2].

High energy regions

Two regions of higher energy peaks were studied. The Gd MNN peaks occur between 600-1250 eV, while the Si KLL peaks are found at 1520-1640 eV. By observation of lineshape changes these peaks were found to be not strongly affected by adventitious oxygen in the chamber. It was in these regions that reliable quantitative results were obtained.

A pronounced change in the Si_{KLL} lineshape was observed upon formation of the rare earth silicide [Figure 5-3]. The 1604 eV peak in that region decays monotonically with increasing Gd content. This feature is believed attributable to a plasmon loss mechanism, and the changes in the lineshape therefore are ascribed to changes in that loss mechanism due to incorporation of Gd.

Quantitative Results

Evaluation of k' (residual error)

After applying the calculated corrections to the dN(E)/dE peak-to-peak intensities, there remained significant disagreement between the AES results and the RBS [Figure 5-4]. Angle-resolved X-ray photoelectron spectroscopy (ARXPS) data indicated that sputter cleaning creates a silicon-rich surface layer of about 10Å. However, the effect on the AES data should be minimized since the flux entering the wide acceptance angle of the AES analyzer is dominated by the signal from near the surface normal. Besides, direct comparison with AES data from samples of the elements shows not only silicon but also Gd at higher concentration than expected.

Normalizing the independent results to 100% total composition (i.e., eliminating the factor of beam current from Eq. 5-1) does not improve the result due to the countervailing senses of the deviations for the Si and the Gd intensities (k'_{Si}, k'_{Gd}). Thus it is reasonable to discuss this disagreement between the RBS and the AES in terms of the model factors N, λ and r.

Linear fit to experimental deviation (k")

The residual error k' was plotted against the corrected AES atomic percent, and empirically fitted with a linear

equation [Figure 5-5]. For the Gd data, the residual error was compensated by a factor k" given by

$$k''_{Gd} = 2.9 - 3.4\,(X_{Gd}^{AES,corr}) \qquad (5\text{-}16)$$

and for Si,

$$k''_{Si} = 0.2 + 0.8\,(X_{Si}^{AES,corr}) \ . \qquad (5\text{-}17)$$

While a more detailed fit to the data is feasible, the large deviation of the error factor from unity (k' varies from 0.4 to 2.8) means that even this very simple approach to a correction term will greatly improve the results.

Results

The results were encouraging [Tables 5-1 and 5-2, Figure 5-4] for films ranging from 50% Si to 100% Si, but the samples near the 1.7:1 stoichiometry of the disilicide phase were not brought into agreement. This group of samples included the bulk disilicide, the reacted thin films, and the codeposited disilicide. It was noted that the deviation of these samples were indicative of excessive Gd and also excessive Si [see Figures 5-4 and 5-5]; though the independent assessment of atomic percent of each element gave a total greater than 100%, the ratio of Si:Gd was very near to the expected 1.7:1.

When the percentages were normalized to total 100% there was good agreement with the RBS analysis throughout the range of compositions, including the anomalous disilicides, with final results in agreement within 1.5 Atom% RMS error.

Discussion

The ratios of the low-energy peaks to the higher-energy peaks (i.e., Si LVV/ Si KLL and Gd NNN/Gd MNN [Figure 5-6] provide evidence that the mean free paths of the Auger electrons is strongly affected by the composition of the sample. Incorporation of gadolinium reduces the intensity of the silicon peaks, with a more severe attenuation of the high energy Si KLL peak compared to the Si LVV. The intensity of the Gd NNN peak is augmented to a greater degree than the Gd MNN.

These observations may be understood as resulting from a shift in the electron mean free path versus kinetic energy curve. For Si, the inclusion of Gd with its numerous shallow core electrons into the matrix produces an abundance of scattering opportunities with respect to elemental silicon, with proportionately more of these energy-loss interactions becoming available for the higher energy KLL electrons. For Gd, the substitution of Si atoms reduces the possibilities of inelastic scattering, and similarly the high-energy Gd MNN peaks have more potential loss-interactions removed by the substitution.

The anomalous AES response of the disilicides could have arisen from a number of factors such an increase in the primary beam, which was measured by biasing the samples. But the close grouping of samples prepared using very different techniques would seem to indicate an intrinsic property of

the disilicide. The AES response for the disilicides is consistent with an increase of ≈20% in the mean free path of the electrons, due to formation of a well-ordered lattice in a narrow composition range with consequent reduced scattering of the photoelectrons.

Conclusion

The introduction of AES equipment with good beam stability and areal resolution along with digital acquisition of E·N(E) spectra provides an opportunity to develop reliable quantitative AES analysis in simple systems. Using standard samples of both elements and compounds (whose compositions are determined by some method of bulk analysis), matrix-sensitive effective sensitivity factors have been derived that provide the means to correct the Auger current measurements and therefore determine compositions quickly and accurately. Qualitative and semi-quantitative information on chemical bonding is also realized from changes in peak shape in the N(E) mode.

Results in the Gd-Si system demonstrate that empirically derived linear relationships based on atom% as measured by AES can yield quite accurate effective sensitivity factors. It is suggested that the measured variation of the effective sensitivity may be readily attributable to one of the first-principle terms in the model equation, and that compilations of such results may

lead to better understanding of AES from the first-principles approach.

In the case of the Gd-Si system, the departure from elemental sensitivities is such that it may be most readily attributable to changes in the inelastic mean free path λ, with differing effects for the Auger energies of the several transitions investigated. The singularity observed in the AES response of the disilicides is consistent with a marked increase in the mean free path of the photoelectrons in the single-phase disilicide compared to mixtures. Further work will be required to substantiate this. However, in the range of composition of this study, quantified compositional information is now readily available from AES.

Table 5-1 Atomic percent silicon and matrix correction factors.
Atomic percent calculated from AES data (Si KLL peak), both the raw peak-to-peak values and matrix-corrected using calculated values. Improved agreement was achieved after applying the empirically derived k'' correction term developed in this work.

Sample	At% Si [RBS]	At% Si [AES]	Corr., k_m	Corr., k''	Norm., to 100%	Km (calc.)	K' (error)	K" (empir.)
Si	100.0	100.0	100.0	100.0	97.6	1.000	1.000	1.000
(a)	93.5	75.6	72.9	93.1	93.5	1.037	0.780	0.783
(b)	82.5	53.5	48.7	82.6	82.7	1.098	0.591	0.590
(c)	73.7	37.3	32.6	70.7	72.4	1.147	0.442	0.460
(d)	63.0	32.6	27.0	64.9	56.2	1.207	0.428	0.416
(e)	63.0	41.4	34.3	72.3	58.5	1.207	0.544	0.474
(f)	63.0	40.5	33.6	71.7	60.5	1.207	0.533	0.469
(g)	63.0	40.1	33.2	71.3	59.5	1.207	0.527	0.466
(h)	63.0	36.3	30.1	68.2	60.3	1.207	0.477	0.440
(i)	60.0	27.1	22.1	58.7	60.6	1.223	0.369	0.377
(j)	50.0	23.6	19.4	54.6	58.3	1.215	0.388	0.355

Table 5-2 Atomic percent gadolinium and matrix correction factors.
Atomic percent calculated from AES data (Gd MNN peak), both the raw peak-to-peak values and matrix-corrected using calculated values. Improved agreement was achieved after applying the empirically derived k'' correction term developed in this work.

Sample	At% Gd [RBS]	At% Gd [AES]	Corr., k_m	Corr., k''	Norm., to 100%	Km (calc.)	K' (error)	K" (empir.)
Si	0.0	5.5	6.6	2.4	2.4	0.829	-.--	2.714
(a)	6.5	13.6	15.8	6.5	6.5	0.860	2.427	2.439
(b)	17.5	29.7	32.6	17.2	17.3	0.910	1.863	1.891
(c)	26.3	39.7	41.8	26.9	27.6	0.950	1.588	1.551
(d)	37.0	53.9	53.9	50.6	43.8	1.000	1.457	1.067
(e)	37.0	54.2	54.2	51.3	41.5	1.000	1.466	1.056
(f)	37.0	52.4	52.4	46.8	39.5	1.000	1.415	1.120
(g)	37.0	53.1	53.1	48.5	40.5	1.000	1.435	1.095
(h)	37.0	51.7	51.3	44.8	39.7	1.007	1.386	1.144
(i)	40.0	48.5	47.8	38.2	39.4	1.014	1.195	1.252
(j)	50.0	49.9	47.0	39.1	41.7	1.060	0.941	1.204

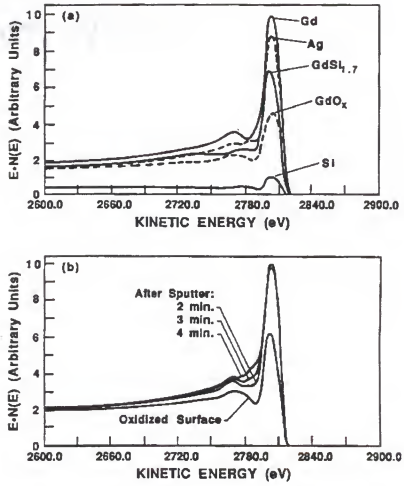

Figure 5-1 Elastic backscattered beam (E_p = 2.8 keV). (a) Elastic peak for various samples (Gd, Ag, $GdSi_{1.7}$, GdO_x, Si); (b) Transients in the elastic peak and characteristic losses, during sputter cleaning (3 keV Ar^+) of air-exposed $GdSi_{1.7}$. Note the immediate increase in the elastic peak intensity upon removal of the oxygen contamination and the development of characteristic loss peaks at ≈12 eV and ≈27 eV below the primary peak.

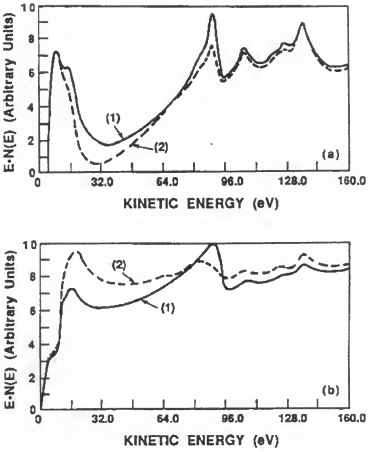

Figure 5-2 Effects of oxygen contamination on gadolinium silicide films [Si LVV/Gd NNN AES region]
(a) (1) clean surface (2) after long-term exposure to residual gas in UHV chamber.
(b) (1) clean film (2) film high in incorporated oxygen during deposition (≈20%)

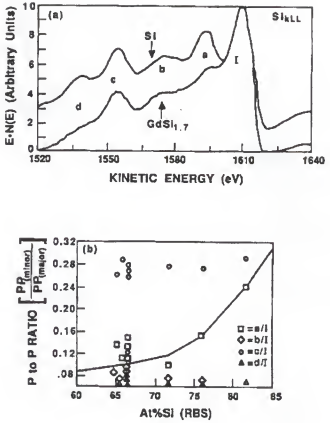

Figure 5-3 Si KLL AES region: (a) Comparison of spectra from elemental Si and from $GdSi_{1.7}$ show a marked quenching of satellite peak 'a'. (b) Fractional intensities of minor peaks in the Si KLL region. Peak 'c' is the KL_1L_1 transition; 'a', 'b' and 'd' are loss peaks. Note the monotonic decay of the loss peak 'a' with increasing Gd content.

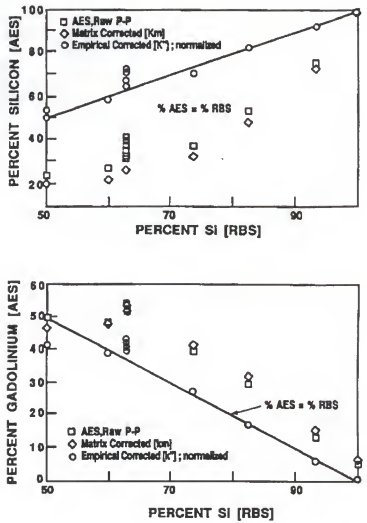

Figure 5-4 AES composition of $GdSi_x$ versus RBS measurements: (AES raw peak-to-peak, matrix corrected, and corrected by empirically derived term k''). (a) Si KLL (b) Gd MNN

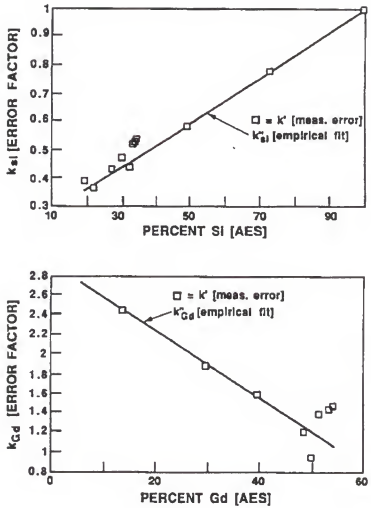

Figure 5-5 Error factor after application of matrix correction terms, and empirical fit k'':
(a) Si KLL (b) Gd MNN

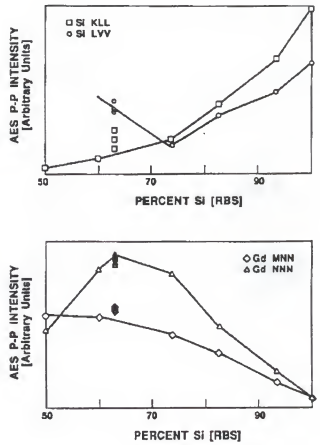

Figure 5-6 Comparison of high energy and low energy AES intensities: (a) Si KLL and LVV (b) Gd MNN and NNN. With increasing Gd content, the lower energy transitions are proportionately higher in intensity compared to the higher energy peaks.

CHAPTER SIX
RESULTS OF ANALYSIS

Crystallization Behavior of Codeposited Films

X-ray Diffraction

Analysis using Cu K_α radiation indicated that the films have an amorphous character as deposited and crystallize to a disilicide structure after a brief anneal at T=400°C. The diffraction pattern then obtained showed a better agreement with the indexed pattern[117] for orthorhombic "$GdSi_2$" than did the reacted thin films [Figure 6-1], indicating a more homogeneous phase formation in the codeposited thin films. A strong reflection at $2\theta=34°$ (d=2.63Å) assigned to orthorhombic $GdSi_2$ (112) indicated a high degree of texturing in the polycrystalline silicide.

Thicker samples (5,000Å) from a well-seasoned sputter target were deposited to increase the diffracted signal intensity. These produced very interesting results in XRD, showing only two very dominant features even before annealing [Figure 6-2, Table 6-1], one near the familiar $GdSi_2$ (112) peak at 34°, and another peak not previously observed near $2\theta=65°$ (d=1.44Å) which could be assigned to $GdSi_2$ (220). The dominance of these peaks is indicative of

two distinct strong preferred orientations in the films. Similar results were obtained with both Si(100) and GaAs(100) substrates.

Rapid annealing (500°C/20 sec.) caused these two peaks to shift to lower angles (larger d-spacings, 1.45Å and 2.65Å respectively). This was consistent with a lattice expansion due to the excess silicon in the deposition (Gd/Si=2). In fact, the $ThSi_2$-type tetragonal phase of $GdSi_2$[83] would have spacings of 2.67Å and 1.45Å for the (112) and (220) reflections [Table 6-2], and it may be nucleated as a metastable form under these conditions.

Annealing at progressively higher temperatures caused these peaks to shift back toward larger 2θ values, with d-spacings reduced to values below the as-deposited values. At temperatures above 700°C these spacings are close to the values calculated for the $(1\bar{1}1)$ and (112) planes in hexagonal AlB_2 $GdSi_{1.7}$ [see Table 6-2]. Considering the crystallographic relationship between the orthogonal or tetragonal half unit cell and the hex unit cell [see Figure 2-1, above], a phase change to hexagonal structure would exhibit related diffraction peaks from these closely related hexagonal planes [Figure 6-3].

The hexagonal $GdSi_{1.7}$ phase as a significant constituent of thin film specimens has previously been observed only for liquid phase reaction of Gd on Si(111) under rapid heating by electron beam.[11,12] Thus its detection in these films on

Si(001) is surprising, and should be understood as tentative without other corroborating diffraction lines. The similarities in the structures and the variation in reported lattice parameters from bulk-sample studies adds to the uncertainty [see above, Table 2-6].

The relative heights of the two peaks varies with time and temperature [Figures 6-4 to 6-7]. For rapid anneals (20 sec. RTA) the 65° peak is quenched dramatically compared to the as-deposited film, then grows slightly with temperature, doubling from 600°C to 800°C but remaining smaller than as-deposited [Figure 6-4, (a)-(e)]. With longer times (40 sec.) the intensity of this peak increases markedly [Figure 6-4, (f) and (g); Figure 6-5] and nears the intensity of the 34° peak.

The 34° peak grows steadily with time and with temperature [Figure 6-6] and begins to develop a slight shoulder at 33.3° (d=2.69Å) that becomes a prominent satellite at 800°C. This satellite is even more prominent in the as-deposited film but is totally quenched by the 500°C treatment.

Furnace treatments (375°, 30 min.) [Figure 6-7] of films on GaAs substrates result in a single major peak at 34° assigned to orthorhombic $GdSi_2$(112), and only a small shoulder on the substrate peak near 64°. On silicon the two peaks occur at larger angles and show nearly equal intensity, more similar to the longer-term RTA heating [see

Figure 6-5(b)]. After 1 hr. at 900°C [Figure 6-7(d)] the 33.3° satellite peak seen in the 800°C RTA data dominates a broad amorphous-type pattern. No clear assignment could be made for this d-spacing.

Treatment at higher temperatures (near 800°C) [Figure 6-4] and for longer times [Figure 6-4, 6-5] also produced broad features at ≈51°, d=1.79Å, which may be assigned to orthorhombic $GdSi_2$ (211) and (121), d=1.78Å and d=1.80Å respectively.

In summary, the strong orientation of these films, especially the single strong (112) orientation observed on the GaAs, indicate that the silicide may form a highly ordered interface with semiconductor substrates. At the same time the phase changes implied by these data and supported by the complex crystallography of the silicides show that much remains to be done before a clear understanding will be reached.

Transmission Electron Microscopy

Attempts to clarify the XRD data using electron diffraction were not very fruitful. Samples were prepared for transmission electron microscopy (TEM) in both the planar and cross-sectional view, revealing a columnar grain structure with grain diameters of ≈500Å [Figures 6-8 to 6-10]. Electron diffraction produced a very spotty ring pattern (polycrystalline), with several bright spots

associated with several individual grains of closely related orientation.

The cross-sectional samples produced had very few transparent areas due to difficulty in thinning the silicide without destroying the substrate support. The high mass absorption of the gadolinium also requires the sections to be quite thin. The few areas available were imaged along the Si(011) and (111) directions in hope of finding silicide crystals with related orientation and planes parallel to the Si(001) surface [Figure 6-8, 6-10].

The columnar grains do not seem to be as singularly oriented as indicated by the XRD data. Several large grains were correlated with plane spacings consistent with the lattice spacing of hexagonal $GdSi_2(1\bar{1}1)$, d=2.61Å [Figure 6-9(d), 6-10(b)]. Some of these grains also showed strong contrast from other distinct planes in nearly the same direction, with a spacing of 2.00Å [Figure 6-10(c)]. This result is not well understood, but could be due to the interpenetration of silicon and gadolinium sublattices with different scattering power. Other grains with lattice spacing 3.37Å could be assigned to hexagonal $GdSi_2(110)$, d=3.37Å [Figure 6-9(c)].

The discrepancy between these data and the XRD results can be tentatively explained by supposing the XRD data are generated by a small number of perfectly oriented grains. With the rest of the columnar grains only slightly out of

alignment with the silicon, very few other reflections would be detected by XRD. The data are thus dominated by the oriented fraction, with the nearly oriented grains essentially transparent to the analysis.

While this explanation is largely conjectural, no other answer offers itself and further investigation will be necessary to resolve the question.

Metallurgical Stability

Stability/Reactivity of Films on Silicon

Dramatic evidence of the role of silicon as the diffusing species in the rare earth/silicon reaction[60] was observed in the codeposited films. In silicon-rich depositions, moderate anneals (RTA 400-600°C, 20 sec.) led to extensive recrystallization of the $GdSi_{1.7}$ phase, with the excess silicon diffusing through a 5,000Å film to the surface where it aggregates [Figure 6-11].

Furnace anneals up to 900°C for one hour produced a massive metallurgical reaction [Figure 6-12], with silicon whiskers growing out of ruptures in a blistering surface oxide. This presents an upper limit to the temperature stability that has not previously been observed. The $GdSi_{1.7}$/Si interface has been reported to be stable up to 900°C.[9]

The low temperature of activation for the rare earth silicide reaction on silicon[45,57] explains the continued

reactivity. It appears that silicide remains intact as a catalytic interface while silicon continues to diffuse through the film and nucleate and grow at the surface in a massive diffusion. The relatively high heat of formation of the silicide[4,118] (comparable to USi_2, ΔHf= -31.2 kCal/mole) [Table 6-3] would prevent its dissolution, while the catalytic effect of the rare earth metal atoms on silicon bonds in the substrate continues to provide free silicon. The defect lattice of the silicide provides a large number of silicon vacancies to enhance diffusion rates through a what is already a relatively open lattice structure. Fortunately, these conditions are beyond device performance limits, but they are conditions that could be approached in processing steps and further investigations are called for.

Stability/Reactivity of Films on GaAs

The recrystallization of silicon-rich films on GaAs is similar to the results on silicon [Figure 6-13]. The composition near the interface may be slightly more Gd-rich, which would be consistent with a predominance of the silicon-deficient orthorhombic phase, as indicated by the XRD data for the GaAs samples.

Both Gd metal and $GdSi_{1.7}$ films were deposited onto GaAs and interface stability was studied upon heating up to 500°C in vacuum. Results for rare earth metals and for rare earth silicides were qualitatively the same, with greatly reduced reactivity in the case of the silicides. AES depth profiles

showed As enrichment at the interface, with a small amount of Ga detected in the silicide [Figure 6-14]. This is consistent with the observed reactivity of rare earth metals with GaAs,[61-65] where As-rare earth bonding is detected at monolayer coverages with the As trapped at the interface, while Ga is observed to diffuse into the metal film in a metallic state.

There is also a slight buildup of silicon at the interface, perhaps promoted by the loss of some Gd to the interface reaction with As. Silicon once nucleated would serve as a sink for excess silicon in the film, especially if the orthorhombic silicide is forming and rejecting excess silicon as evidenced by the AES profiles.

Effects of Oxygen

Oxygen Behavior in the Thin Film Reaction

All rare earth metals have highly exothermic reactions with oxygen, even compared to the group IVA transition metals [see Table 6-4]. The ability of gadolinium to reduce SiO_2 was evident in our attempts to crystallize cosputtered films deposited on quartz. Hot stage XRD under flowing He yielded no silicide peaks, with complete oxidation of the film as low as 400°C.

AES can provide depth information by either sputter depth profiles or by SAM line-scans of craters from stationary ion-beams.[119] Results for partially-reacted thin

films showed that O was rejected from the silicide and concentrated in the unreacted rare earth metal [Figure 6-15]; this suggests that the silicides should be good diffusion barriers for O.

These profiles also confirm a mechanism proposed to explain the critical-temperature reaction kinetics of the thin film reaction.[57] Any thin surface oxide of silicon would be reducible by the rare earth metal, creating a high level of oxygen in the rare earth metal that is further increased by the advancing silicide interface. A thin barrier layer of oxide in the rare earth metal is thus created, hindering the diffusion of silicon into the metal. This transfer of oxygen to the rare earth metal is confirmed in our samples.

The high oxygen level was capable of stopping the reaction, approaching a concentration sufficient to nucleate GdO (ΔHf= -17 kCal/mole) but not the higher oxide Gd_2O_3 (ΔHf= -434.9 kCal/mole), which is highly stable[118] [see Table 6-4]. The formation of an interfacial layer of GdO at the silicide interface, promoted when silicide has begun to form, is the inhibitor of silicide formation at lower temperatures. This oxide has a low heat of formation compared to the silicide, so its break-up is energetically favored, and proceeds at higher temperatures.

The delay in the onset of silicide formation has also been attributed to the presence of a carbon contamination

layer.[58] In either case, a higher activation temperature is required to dissolve or "punch through" the oxide layer, with the silicide reaction proceeding to completion within minutes.

Behavior of Oxygen in Codeposited Films

Oxygen contamination of the codeposited films was frequently excessive due to repeated exposure of the sputter target to the atmosphere in the process of loading samples. The effect of this contamination was most readily observed in sheet resistance measurements [discussed below], but it can be expected that contact properties were affected as well. Changing the apparatus to allow sample introduction while maintaining a high vacuum in the target chamber would be highly desirable.

AES analysis also showed that film oxidation in the ambient produced a surface oxide rich in silicon, while heat treatment under a reducing atmosphere in either RTA or a tube furnace produced a gadolinium-rich surface oxide. The gadolinium silicide samples appear to be protected against extensive oxidation similarly to $ErSi_2$, which is stable against oxidation at about 400°C.[75]

Electrical and Contact Properties

Resistivity

Sheet resistance measurements using the four-point probe technique were taken before and after heat treatment,

with improved conductivity for the annealed films. Using thickness measurements from a quartz deposition monitor as well as profilometry data allowed calculation of the specific resistivity of the silicide. The sheet resistance of the films was about 17 ohms/square when 1500Å were deposited; this yields a resistivity of 250μΩ-cm that is consistent with reported values of reacted thin films and bulk silicides[9,45,56,71] [see Tables 2-4, 2-5, above]. Resistivity was not a strong function of Si:Gd ratio, but increased to ≈500μΩ-cm with oxygen content of ≈10%.

Resistivity in metal silicides has been related to bond lengths in the silicide,[5] with lower resistivity observed where metal-silicon distances are shorter compared to metal-metal or silicon-silicon distances. For orthorhombic $GdSi_{1.7}$, these distances [Table 6-5] are consistent with higher resistivity. A larger grain size in the recrystallized films would no doubt improve the measured resistivity. However, gadolinium is among the most resistive of rare earth metals [see Table 2-5, above], and other rare earths may offer considerably improved conductivity.

Contact Properties--Silicon (100)

Dot contacts (0.7mm diameter) for I-V measurements were fabricated by mechanical masks using moderately-doped silicon ($n_b \approx 4 \times 10^{17}$) of both n- and p-type. The Schottky barrier height on p-Si was ≈0.70 eV (n = 1.35), in agreement

with the previously reported value. For n-Si the I-V showed a very low barrier, consistent with the reported value of 0.37 eV[6] [Figure 6-16]. Measurements of Schottky barrier heights for the rare earth silicides are difficult to obtain from log(I) vs. V data because of the effects of high series resistance and observed high recombination currents in these contacts.[10,75]

The difficulty in obtaining barrier heights from I-V measurements and high ideality factors for these silicides has been attributed to the formation of parallel diodes with a combination of high and low barrier heights.[120,121] In such cases, regions of the contact having low barrier heights will dominate the conduction even if they comprise a small percent of the total contact area. With the increased presence of large oriented grains in the codeposited films such orientation effects may be even more predominant for our samples. Such nonuniform contacts could also explain the above-mentioned high leakage currents observed in rare earth silicide contacts.

For more highly doped substrates of both polarities, ohmic behavior became predominant with little or no heat treatment, suggesting that the films reacted with the sputter-cleaned substrates due to heating during deposition. The substrates were not cooled and temperature was not monitored during the deposition.

Contact Properties--GaAs (100)

Dot patterns for diode testing were prepared in the same fashion on GaAs substrates of moderate doping levels (n_b=4x10^{17}), with back contacts of annealed Au-Ge on the n-GaAs and large-area silicide contacts to approximate ohmic behavior for the p-type samples.

Contacts to both n- and p-type GaAs were initially rectifying. Barrier heights were not obtained, with very high ideality factors being found (n>2) for short linear segments in the Log(I) vs. V plots [Figure 6-17]. Because recrystallization of the silicide on GaAs showed even greater orientation effects than on silicon, the comments above concerning contacts of mixed barrier heights is even more important for the case of GaAs.

Brief anneals (600°C/10 sec.) produced large currents with similar current response in forward and reverse bias. In particular for the case of more highly doped substrates the contacts appear to become near ohmic to both n- and p-type, although results were uneven. The decay of the barrier properties and increased reverse current with heat treatment are similar to previous results with Pd on GaAs.[20] In this case the same arguments for field emission[122] might be applied, but with indiffusing Si as the dopant and without the incursions of reactive metal that give a geometrical enhancement of the field emission for the Pd contacts.

Several conflicting theories of Schottky barrier formation continue to be discussed in the literature.[66-70] With respect to this work, the role of interface compound formation may be emphasized for two reasons. Real contacts and particularly ohmic contacts depend upon a certain degree of reactive metallurgy, with extensive interfacial reaction products that obviate the abrupt interface model presented in studies directed at pure Schottky behavior. Secondly, in order to eliminate surface oxides and contaminants as much as possible the substrates were presputtered before depositing the silicide. Sputtering is known to produced altered surface composition[123] and broken bonds that will promote interfacial reaction.

It was shown above that the annealed $GdSi_{1.7}$/GaAs interface was As- and Gd-rich, with small amounts of Ga dispersed in the film, consistent with previous studies of rare earth metals on GaAs.[61-65] These studies showed strong arsenide-like bonding, including the identification of an interface phase comparable to bulk CeAs in photoemission studies.[62] For the GaAs substrates in this study, free As existing on the sputtered surface[123] would also favor the formation of an arsenide.

The properties of a GdAs interfacial compound is an intriguing one. The rare earth monopnictides (RX, R = rare earth metal, X = N, P, As, Sb) have attracted interest because of their electrical and magnetic properties.[124,125]

Calculated band structures for the gadolinium monopnictides indicate very low effective masses for holes ($0.1m_o$ to $0.3m_o$) and electrons ($0.1m_o$ in the S and Z directions).[126]

The contact properties of GdAs on GaAs are not known, but they merit investigation. The effects of such a compound at the $GdSi_{1.7}$/GaAs interface may be involved in the contact properties and must be considered. GdAs melts above 2270°C[127] and rare earth arsenides are formed quite exothermically (HoAs: ΔHf= -72 kCal/mole[118]) [Table 6-6].

Overall, the results for GaAs have been inconsistent and unenlightening. The effects of incorporated oxygen in the films may also have a more serious effect here than in the case for silicon. However, the possibilities to be realized from a highly oriented refractory film with an interface of limited reactivity with respect to the GaAs suggest that further work is warranted.

Problems in Patterning and Probing

Electrical measurements of rare earth silicide contacts formed by codeposition are severely hampered by the difficulty in patterning the silicide. Once formed, the silicide is more resistant to chemical etches than the substrate material. As-deposited amorphous mixtures with a low ratio of Si/Gd were found to be soluble in HNO_3 solutions, but stoichiometric films near the correct 1.7:1 ratio were not attacked. Deposition from a sputter source subjects photoresist layers to polymerization by energetic

particles and heat, while the wide angular distribution of flux from a large-area target does not produce the clean edges needed for effective liftoff. For this reason, we were unable to produce suitable patterns for measuring contact resistance.

The silicide is also difficult to probe electrically, due to its hardness and the presence of a surface oxide. Overlayers of softer conductive metals helped with this problem, but introduced more variables to the question of contact properties.

Optical Properties

The filling of the shielded 4f electron shells in the lanthanide sequence leads to a number of anomalous properties of rare earth compounds, including in some cases optical absorption spectra that exhibit discrete lines that are more typical of atomic or gaseous absorption than the band absorption of solids.[2] Thin layers of Yb metal have been investigated as transparent top contacts for MIS solar cells.[128] It was therefore reasonable to investigate for potentially advantageous optical properties of the rare earth silicides, studies of which have not appeared in the literature to date.

The optical reflectance of reacted $GdSi_{1.7}$ on Si substrates was measured and a drop in reflectance for wavelengths near 450nm was detected [Figure 6-18]. This suggests that the $GdSi_{1.7}$ has some optical transmission in

the near ultra-violet and blue region of the spectrum. This is further substantiated by the fact that optical interference bands have been observed for 1000Å $GdSi_{1.7}$ films on Si where the layer was thinned by argon ion sputtering for AES depth profiling [Figure 6-19]. The interference band moved with the wavelength of monochromatic light and could be seen for wavelengths as long as the green region. The transparency observed may be assisted by incorporation of residual oxygen in the silicide.

Optical transmission measured on semi-opaque 400Å and 800Å films indicate that any useful transparency is confined to very thin and hence very resistive layers. Together with the reflectance data, these data are consistent with an optical absorption length on the order of 400Å. Ellipsometry measurements (λ = 6328Å) yielded real and imaginary components of the index of refraction similar to $NiSi_2$[129] [Table 6-7].

Table 6-1 X-ray diffraction peak position (2θ) and d-spacing for 5,000Å $GdSi_2$ film after various heat treatments.

Sample treatment	$2\theta_1$	d[Å]	$2\theta_2$	d[Å]
As deposited	34.2	2.621	64.9	1.437
500°C/20 sec. (RTA)	33.9	2.644	64.1	1.453
600°C/20 sec. (RTA)	34.1	2.630	64.4	1.447
700°C/20 sec. (RTA)	34.3	2.614	65.0	1.435
800°C/20 sec. (RTA)	34.4	2.607	65.5	1.425
600°C/40 sec. (RTA)	34.3	2.614	64.7	1.44
800°C/40 sec. (RTA)	34.4	2.607	65.3	1.429
375°C/30 min. furn.	34.4	2.607	64.7	1.44
GaAs, 375°C/30 min.	34.0	2.637	64.1	1.449

Table 6-2 Equivalent lattice planes and d-spacings, calculated for the three reported structures of $GdSi_x$ ($1.7 \leq x \leq 2$), using lattice parameters from various cited references (see Table 4-6).

Crystal type	hkl	d[Å]	hkl	d[Å]	ref.
Tetragonal	(112)	2.67	(220)	1.45	83
Orthogonal	(112)	2.63	(220)	1.432	86
		2.626		1.427	80
Hexagonal	(1$\underline{1}$1)	2.615	(112)	1.420	87
		2.606		1.414	80

Table 6-3 Heats of formation for silicides.

Silicide	ΔH_f/mole [kCal]	ref.
$NiSi_2$	-20.7	4
WSi_2	-22.5	4
$TaSi_2$	-24.0	4
$CoSi_2$	-24.6	4
$MoSi_2$	-27.9	4
$TiSi_2$	-32.1	4
$LaSi_2$	-43.8	4
USi_2	-31.2	118

Table 6-4 Heats of formation for oxides.

Oxide	ΔH_f/mole [kCal]	ΔH_f per oxygen	ref.
Sc_2O_3	-411.0	-137	4
Y_2O_3	-455.5	-152	4
La_2O_3	-428.5	-143	4
Gd_2O_3	-434.9	-145	118
Al_2O_3	-400	-133	118
ZrO_2	-261.6	-131	4
TiO_2	-219.0	-110	4
SiO_2	-206	-103	118
Ta_2O_5	-499.8	-100	4
Nb_2O_5	-462.7	-92.5	4
WO_3	-200.8	-66.9	4
CrO_3	-136.8	-45.6	4
As_2O_5	-221.05	-44.2	118
Ga_2O_3	-260.3	-86.7	118
Ga_2O	-85	-85	118

Table 6-5 Bond lengths: (a) Calculated [this work] for orthorhombic $GdSi_{1.7}$; (b) $ThSi_2$; (c) silicon-silicon bonds, related disilicides.

(a)

$GdSi_2$ (orth.) Bond type:	length 1 [Å]	length 2 [Å]
metal-metal	2.71	
metal-silicon	2.95	3.07
silicon-silicon	2.22	2.39

(b)

$ThSi_2$ Bond type:	Tetrag. l,[Å]	Hexag. l,[Å]	ref.
metal-metal	4.135	4.126	82
metal-silicon	3.161	3.155	82
silicon-silicon	2.39	2.31	85

(c)

Silicide	Tetrag. l,[Å]	Hexag. l,[Å]	ref.
USi_2	2.28	2.225	85
$PuSi_2$	2.26	2.24	85
YSi_2	2.23	2.225	85

Table 6-6 Heats of formation and melting temperatures, rare earth arsenides.

Arsenide	ΔH_f/mole [kCal]	ref.
HoAs	-72	118
GaAs	-17	118

Arsenide	T_m	ref.
GdAs	>2270C°	127

Table 6-7 Real and imaginary coefficients of the index of refraction measured for various silicides (λ=6328Å).

Silicide	n	k	ref.
$GdSi_2$	2.85	2.7	[PW]
NiSi	2.89	2.87	129
$MoSi_2$	4.16	1.44	129
$NiSi_2$	3.37	2.44	129
$CrSi_2$	2.98	2.13	129
WSi_2	4.42	1.68	129
Ir_3Si_5	4.50	1.70	129
ReSi	3.68	1.53	129
$CoSi_2$	2.13	1.28	129

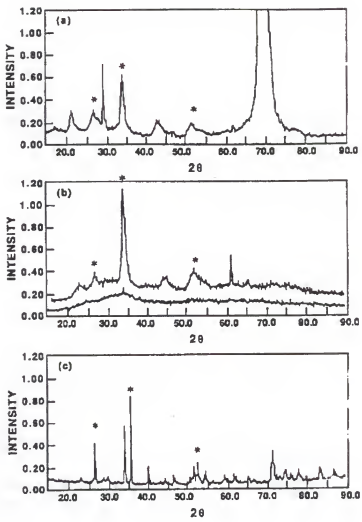

Figure 6-1 X-ray diffraction data: strong peaks identified with the orthorhombic $GdSi_{1.7}$ are indicated.
(a) 2000Å Gd deposited on Si, heated 400°C (fully reacted)
(b) Codeposition, both amorphous as-deposited and after annealing at 400°C.
(c) Powder pattern, bulk-prepared $GdSi_2$

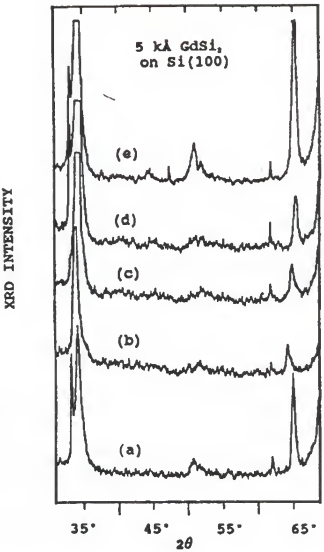

Figure 6-2 X-ray diffraction data for $GdSi_2$ film after rapid thermal annealing (RTA):
(a) As deposited (b) 500°C/20 sec. (c) 700°C/20 sec.
(d) 800°C/20 sec. (e) 800°C/40 sec.
Thicker films show two very dominant features [Table 4.3 XRD data], one near the familiar $GdSi_2$ (112) peak at 34° and another near 2θ=65° (d=1.44Å) which could be assigned to $GdSi_2$ (220). The dominance of these peaks is indicative of two distinct strong preferred orientations in the films.

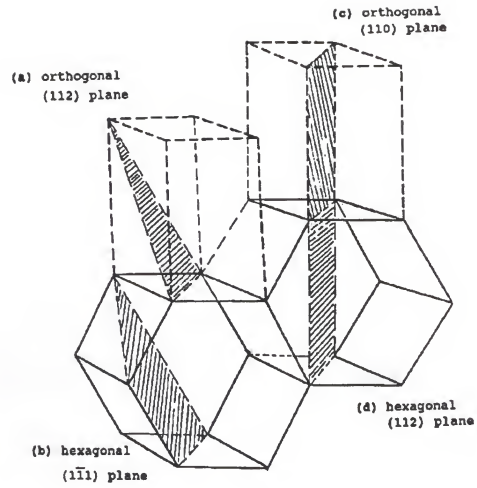

Figure 6-3 Juxtaposition of the hexagonal unit cell and the orthogonal/tetragonal half-unit cell, showing closely-related planes.
(a) orthogonal (112), (b) hexagonal (1$\bar{1}$1) planes;
(c) orthogonal (110), (d) hexagonal (112) planes.

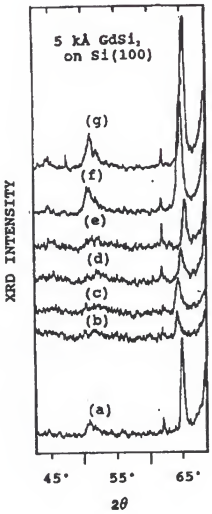

Figure 6-4 Expanded view of x-ray diffraction data for $GdSi_2$ film after rapid thermal annealing (RTA):
(a) As deposited (b) 500°C/20 sec. (c) 600°C/20 sec.
(d) 700°C/20 sec. (e) 800°C/20 sec. (f) 600°C/40 sec.
(g) 800°C/40 sec.
For the briefer 20 sec. anneals, [(a)-(e)], the 65° peak is quenched dramatically compared to the as-deposited film, then grows slightly with temperature, doubling from 600°C to 800°C but remaining smaller than as-deposited (a). Longer anneals cause a pronounced increase in the peak intensity [(f), (g)]. The marked shift to larger angle suggests a phase change to hexagonal $GdSi_2$.

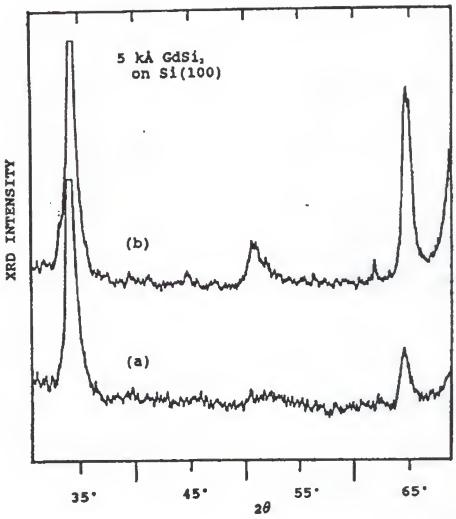

Figure 6-5 X-ray diffraction data for $GdSi_2$ film after rapid thermal annealing (RTA) for different times: (a) 600°C/20 sec. (b) 600°C/40 sec.
With longer time at temperature, the 65° peak increases markedly and nears the intensity of the 34° peak, indicating a time threshold for growth of the grains contributing to the 65° peak.

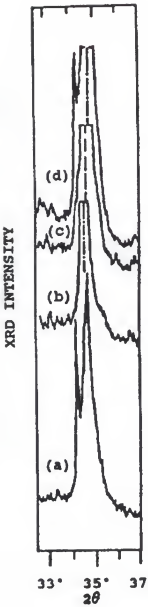

Figure 6-6 Expanded section of x-ray diffraction data for $GdSi_2$ film after rapid thermal annealing:
(a) As deposited (b) 500°C/20 sec.
(c) 700°C/20 sec. (d) 800°C/20 sec.
The 34° peak increases in intensity with temperature, and appears at steadily increasing angles after an initial shift to lower angle after heating at 500°C. A distinct satellite peak at 33.3° (d=2.69Å) in the as-deposited film is totally quenched by the 500°C treatment. At higher temperatures it reappears as a slight shoulder on the larger peak, becoming again a prominent satellite at 800°C.

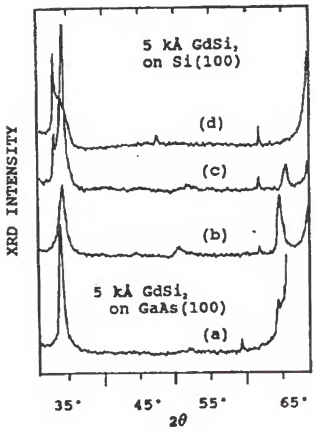

Figure 6-7 X-ray diffraction data for $GdSi_2$ film after furnace heat treatments (375°C, 30 min.).
(a) On a GaAs substrate the XRD data are dominated by a 34° peak assigned to orthorhombic $GdSi_2$(112), with a small peak appearing at 64° as a satellite on the shoulder of the substrate peak.
(b) On silicon the two peaks occur at larger angles and at nearly equal intensity.
(c) A spectrum from a 800°C/20 sec. RTA anneal is included for comparison, showing the predominance of the 34° peak for briefer anneals, and the continued shift of the 65° peak to larger angles at higher temperatures.
(d) After 1 hr. at 900°C a 33.3° peak, appearing as a satellite in the 800°C data, dominates a broad amorphous-type pattern. No clear assignment could be made for this d-spacing.

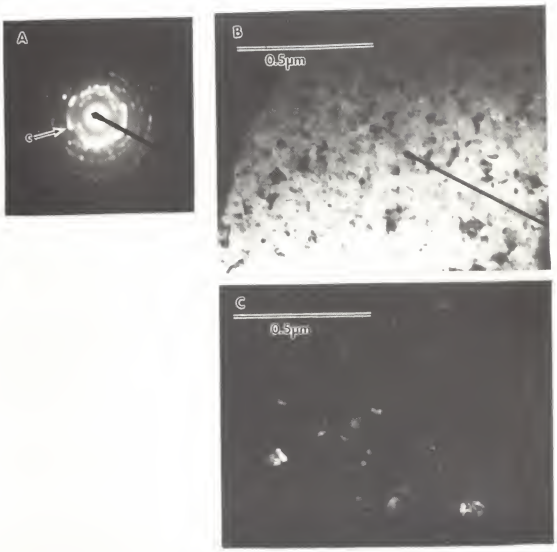

Figure 6-8 Planar TEM photo.
(a) Electron diffraction produced a very spotty ring pattern (polycrystalline). (b) Bright field (BF) and (c) dark field (DF) images produced from the indicated bright spot in (a). The grains appearing in DF are imaged with lattice spacings of ≈2.6Å.

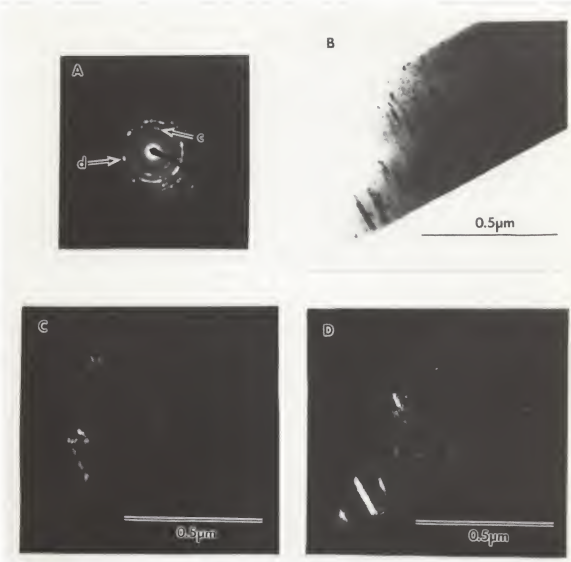

Figure 6-9 Cross-sectional TEM of $GdSi_2$ film (800C° RTA anneal). The camera axis is along the substrate (011) direction.
(a) Electron diffraction pattern shows spotty rings (polycrystalline).
(b) Bright field image
(c) Dark field (DF) image from spot C, lattice spacing 3.37Å (hexagonal $GdSi_2(110)$).
(d) DF image from spot D, lattice spacing 2.61Å (hexagonal $GdSi_2(1\bar{1}1)$).

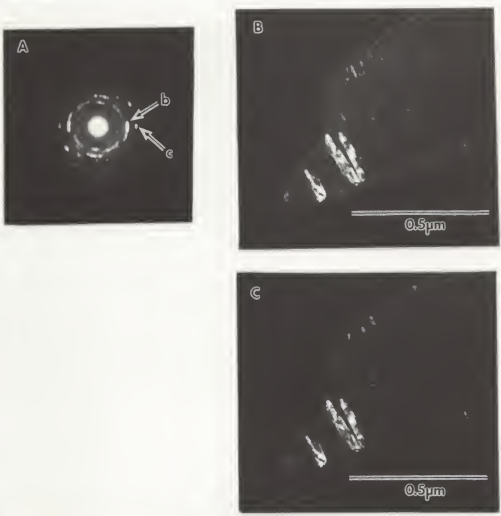

Figure 6-10 Cross-sectional TEM of $GdSi_2$ film (800°C RTA anneal). The camera axis is along the substrate (111) direction.
(a) Electron diffraction pattern shows spotty rings (polycrystalline) with groupings of strong spots.
(b) Dark field (DF) image from spot B, lattice spacing 2.61Å.
(c) DF image from spot C, lattice spacing 2.00Å; the same grains appearing as in (b).

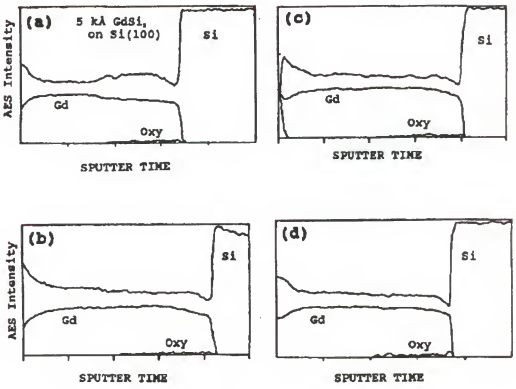

Figure 6-11 Auger depth profiles of codeposited $GdSi_x$ films, x=2 (silicon-rich), showing change to 1.7:1 stoichiometry after annealing.
(a) as deposited; (b) 500°C/20 sec.,
(c) 800C°/40 sec. (RTA); (d) 375C°/1 hr. (furnace).

Figure 6-12 SEM photo of $GdSi_2$ film after furnace anneal at 900°C for one hour, showing a massive metallurgical reaction that produced silicon whiskers growing out of ruptures in a blistering surface oxide.

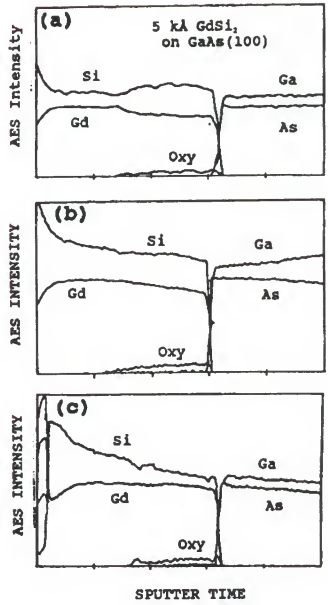

Figure 6-13 Auger depth profiles of codeposited $GdSi_x$ films, x=2 (silicon-rich), on GaAs substrates, showing change to 1.7:1 stoichiometry after anneal.
(a) as deposited (b) 500°C/20 sec. RTA
(c) 700C°/20 sec. RTA

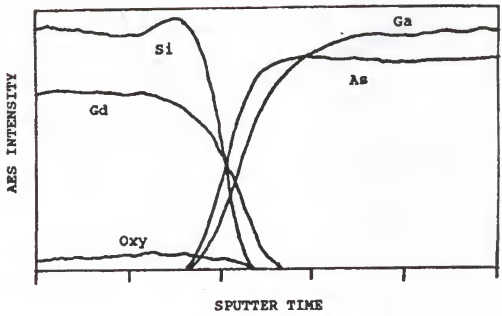

Figure 6-14 Expanded view of Auger depth profile of annealed $GdSi_2$ film on GaAs, showing an As-rich interface with a small amount of Ga detected in the silicide. Excess silicon is accumulated in the film above the interface due to the loss of Gd in the interface reaction.

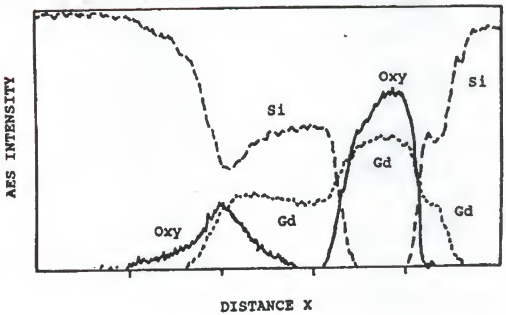

Figure 6-15 Auger line scan across the edge of a fixed ion-beam sputter crater in a partially-reacted Gd film on silicon. Oxygen rejected from the reacted (silicide) region accumulates in the remaining Gd metal, leading to the formation of GdO.

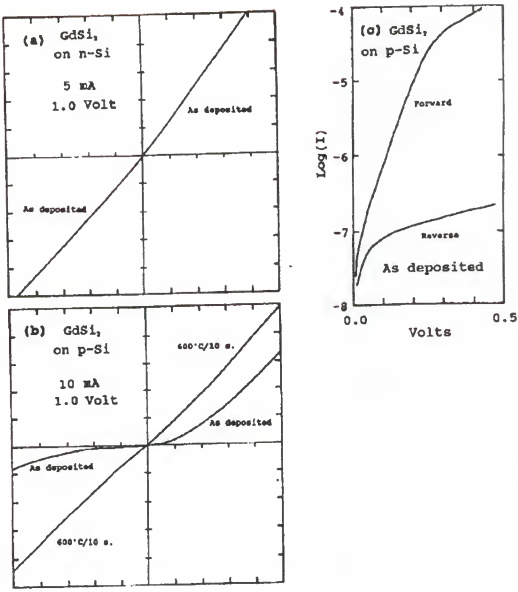

Figure 6-16 Current-voltage measurements of $GdSi_2$ contacts on silicon.
(a) On n-type silicon - ohmic as deposited.
(b) On p-type silicon - rectifying as deposited, but near-ohmic after anneal of 600°C/10 sec.
(c) Log(I) vs. V plot for contact to p-silicon. Schottky barrier height measurements from these data are not truly meaningful due to high reverse current and large ideality factor (n=1.35).

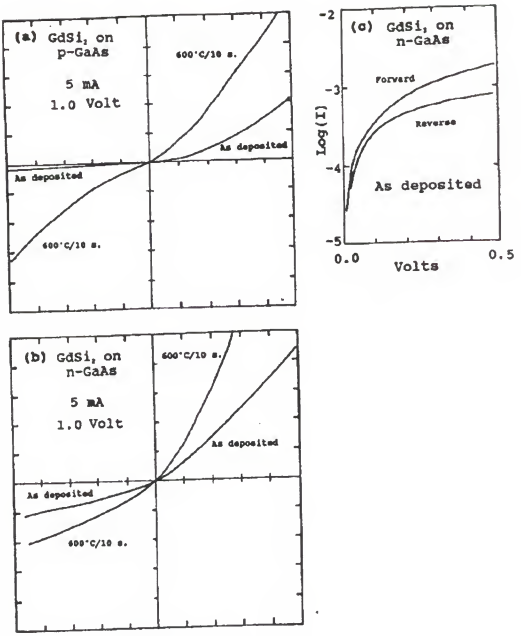

Figure 6-17 Current-voltage data, $GdSi_2$ contacts on GaAs.
(a) Contacts to p-GaAs begin to show ohmicity after anneal of 600°C/10 sec.
(b) On n-GaAs, rectifying properties persist after anneal. Ohmicity was attained for more highly doped samples.
(c) Log(I) vs. V plot for contact to n-GaAs. The lack of a significant linear segment and high reverse current make measurements of Schottky barrier height from these data problematical.

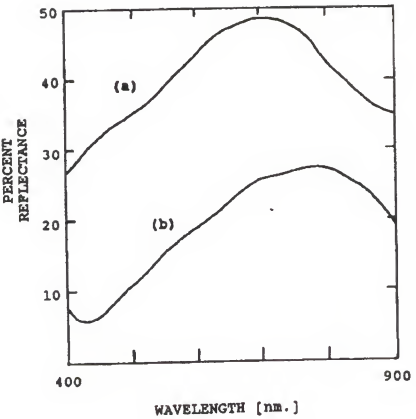

Figure 6-18 Optical reflectance of reacted $GdSi_{1.7}$ on Si substrates showing a drop in reflectance for wavelengths near 450nm.
(a) Reflectance from Gd metal film.
(b) Reflectance from $GdSi_{1.7}$ film.

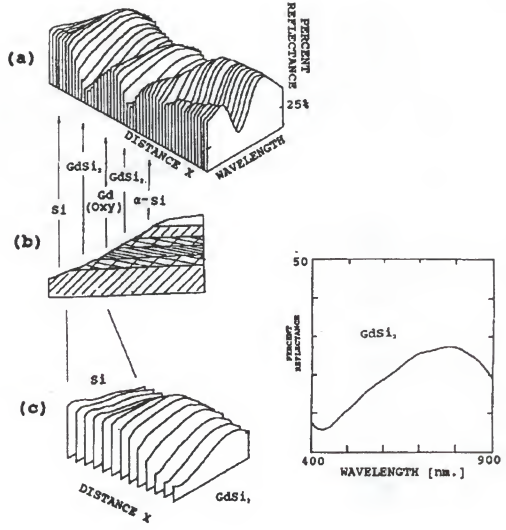

Figure 6-19 Reflectance measurements of small (50 μm) spot size.

(a) A series of reflectance vs. wavelength data taken by stepping along the edge of a stationary ion beam sputter crater in a partially-reacted multilayer sample (see Figure 5-5) consisting of $Si/GdSi_2/Gd/GdSi_{1.7}/\alpha$-Si.

(b) Schematic diagram of the exposed layers.

(c) Expanded portion of the optical data showing the transition from substrate silicon to reflectance typical of $GdSi_{1.7}$, comparable to the data at the right from a codeposited $GdSi_{1.7}$ film.

CHAPTER SEVEN
CONCLUSION

For several reasons, the rare earth silicides are promising as semiconductor contact materials for solar cell applications. They have some of the lowest Schottky barrier heights measured to date for n-silicon. The silicides are high-melting, refractory materials with reasonable electrical conductivity that form reasonably stable interfaces with silicon and GaAs substrates. Ohmic contacts to n-Si are readily achieved, and the potential to form such contacts with epitaxial silicides is an attractive one.

Several modes of rare earth silicide deposition have been investigated, leading to a capability of sputter depositing a stoichiometric mixture of Gd and Si with a low level of incorporated impurity, which recrystallizes in a disilicide structure with a moderate annealing. The rough surface of reacted silicides has been eliminated by the codeposition technique, and silicide films are now readily deposited on non-silicon substrates. The problems with oxygen contamination have been shown to be manageable, although improved consistency in film quality could be achieved by changes in the apparatus to eliminate repeated venting to atmosphere during sample introduction.

The as-deposited and heat-treated films show a strong orientation with evidence of the hexagonal phase being formed on Si(100), which has not been previously observed. Intrinsic optical and electrical properties of these codeposited films have been measured, as well as contact properties on both n- and p-type silicon consistent with those reported in the literature.

In the course of this study, two novel methods of data reduction were developed that greatly improve the measurement of surface composition from electron spectroscopies. Composition profiles derived from angle-resolved XPS data give new insight into the effects of ion bombardment on compounds, and discerned layered surface oxides on air-exposed substrates. In addition, matrix-corrected AES sensitivity factors were developed which facilitate monitoring of the composition for such mixed films.

Unfortunately, the resistance of the silicides to etching and resultant difficulty in patterning has prevented measurement of contact resistance even for the case of n-Si. A full understanding of the contacts, including interfacial reaction with GaAs, and optimization of contact properties has not been realized.

These silicides may yet be found useful in improving the performance of solar cells. Their potential as ohmic contacts to GaAs has not been fully developed. The strong

orientation effects observed indicate the potential for improving contact properties by increasing the area of well-ordered interface associated with the oriented phase. Such well-ordered and oriented silicide films may have value as barriers to oxidation or as diffusion barriers for other conductive or distributive metallizations, thus extending the lifetime of solar cell devices. Demonstrated problems with oxidation of $Al_xGa_{1-x}As$ window layers[130] indicate that consideration of rare earth silicides as protective barrier layers may be justified independent of any role in reducing contact resistance.

REFERENCE LIST

1. T. Moeller, The Chemistry of the Lanthanides (Reinhold, New York, 1963).

2. D. M. Yost, H. R. Russell, and C. S. Garner, The Rare Earth Elements and their Compounds (John Wiley & Sons, Inc., New York, 1947), Chap. 3.

3. R. R. Heikes, "Theory of electron-transport properties of the 4-f electrons in rare earth compounds", in Rare Earth Research, edited by E. V. Kleber (Macmillan, New York, 1961), p.247.

4. M-A. Nicollet and S. S. Lau, "Formation and Characterization of Transition-Metal Silicides", in VLSI Electronics Microstructure Science, edited by N. G. Einspruch and G. B. Larrabee (Academic Press, New York, 1983), vol. 6, p.329.

5. S. P. Murarka, J. Vac. Sci. Technol. 17, 775 (1980).

6. K. N. Tu, R. D. Thompson, and B. Y. Tsaur, Appl. Phys. Lett. 38(8), 626 (1981).

7. H. Norde, J. deSousa Pires, F. D'Heurle, F. Pesavento, S. Petersson and P. A. Tove, Appl. Phys. Lett. 38(11), 865 (1981).

8. N. Braslau, Thin Solid Films 104, 391 (1983).

9. R. D. Thompson, B. Y. Tsaur, and K. N. Tu, Appl. Phys. Lett. 38(7), 535 (1981).

10. V. M. Koleshko, V. F. Belitsky and A. A. Khodin, Th. Sol. Films 141, 277 (1986).

11. J. A. Knapp and S. T. Picraux, Appl. Phys. Lett. 48(7), 467 (1986).

12. J. A. Knapp and S. T. Picraux, Mat. Res. Soc. Symp. Proc. 54, 261 (1986).

13. I. Gercôs, G. Molnar, E. Jaroli, E. Zsoldos, G. Petô, J. Gyulai and E. Bugiel, Appl. Phys. Lett. 51(25), 2144 (1987).

14. S. P. Murarka, Silicides for VLSI Applications (Academic Press, New York, 1983).

15. P. B. Ghate and C. R. Fuller, "Multilevel interconnections for VLSI", in Semiconductor Silicon--1981, edited by H. Huff, R. Kriegler, and Y. Takeishi (Electrochem. Soc., Princeton, New Jersey, 1981), p.680.

16. S. Kritzinger and K. N. Tu, J. Appl. Phys. 37, 205 (1980).

17. M. Eizenberg, H. Foll, and K. N. Tu, Appl. Phys. Lett. 37, 547 (1980).

18. D. Shinoda, "Ohmic contacts to silicon using evaporated metal silicides", in Ohmic Contacts to Semiconductors, edited by B. Schwartz (Electrochem. Soc., Princeton, 1969), p.200.

19. S. M. Sze, Physics of Semiconductor Devices, 2nd ed. (Wiley, New York, 1981).

20. A. K. Sinha, T. E. Smith, and H. J. Levinstein, IEEE Transactions on Electron Devices ED22, 218 (1975).

21. H. B. Michaelson, IBM J. Res. Develop. 22(1), 72 (1978).

22. L. J. Brillson, Phys. Rev. Lett. 40, 260 (1978).

23. J. Bardeen, Phys. Rev. 71(10), 717 (1947).

24. I. Ohdomari, T. S. Kuan, and K. N. Tu, J. Appl. Phys. 50, 7020 (1979).

25. M. J. Turner and E. H. Rhoderick, Solid State Electron. 11, 291 (1968).

26. J. L. Freeouf, J. Vac. Sci. Technol. 18, 910 (1981).

27. J. M. Andrews and J. C. Phillips, Phys. Rev. Lett. 35, 56 (1975).

28. G. Ottaviani and K. N. Tu, Phys. Rev. Lett. 44(4), 284 (1980).

29. R. E. Hummel, Electronic Properties of Materials (Springer-Verlag, New York, 1985).

30. C. Y. Chang, Y. K. Fang, and S. M. Sze, Solid-State Electron. 14, 541 (1971).

31. A. Piotrowska, A. Guivarch and G. Pelous, Solid-State Electron. 26(3), 179 (1983).

32. T. M. Reith and J. D. Schick, Appl. Phys. Lett. 25, 524 (1974).

33. N. Braslau, J. B. Gunn, and J. Staples, Solid-State Electron. 10, 381 (1967).

34. M. Finetti, P. Ostoja, S. Solmi, and G. Soncini, Solid-State Electron. 23, 255 (1980).

35. J. McCarthy, Microelectronics and Reliability 9, 187 (1970).

36. D. K. Schroder and D. L. Meier, IEEE Transactions on Electron Devices ED-31(5), 637 (1984).

37. J. M. Andrews, J. Vac. Sci. Technol. 11, 972 (1974).

38. G. J. Van Gurp, J. Appl. Phys. 46, 4308 (1975).

39. S. S. Cohen, Thin Solid Films 104, 361 (1983).

40. H. H. Berger, J. Electrochem. Soc. 119(4), 507 (1972).

41. D. L. Meier and D. K. Schroder, IEEE Transactions on Electron Devices ED-31(5), 647 (1984).

42. S. J. Proctor and L. W. Linholm, IEEE Electron Device Letters EDL-3(10), 294 (1982).

43. W. M. Loh, S. E. Swirhun, T. A. Schreyer, R. M. Swanson and K. C. Saraswat, IEEE Transactions on Electron Devices ED-34(3), 512 (1987).

44. H. Murrmann and D. Widmann, IEEE Transactions on Electron Devices ED-16(12), 1022 (1969).

45. R. D. Thompson and K. N. Tu, Thin Sol. Films 93, 265 (1982).

46. S. P. Murarka and D. B. Fraser, J. Appl. Phys. 51, 350 (1980).

47. S. P. Murarka, D. B. Fraser, T. F. Retajczyk, Jr., and T. T. Sheng, J. Appl. Phys. 51, 5380 (1980).

48. T. F. Retajczyk, Jr., and A. K. Sinha, Thin Solid Films 70, 241 (1980).

49. S. P. Murarka and D. B. Fraser, J. Appl. Phys. 51, 342 (1980).

50. J. Angilello, F. d'Heurle, S. Peterson, and A. Segmüller, J. Vac. Sci. Technol. 17, 471 (1980).

51. H. Ishiwara, K. Hikosaka, and S. Furukawa, J. Appl. Phys. 50, 5304 (1979).

52. K. C. R. Chiu, J. M. Poate, J. E. Rowe, T. T. Sheng, and A. G. Cullis, Appl. Phys. Lett. 38, 988 (1981).

53. M. Iwami, K. Okuno, S. Kamei, T. Ito, and A. Hiraki, J. Electrochem. Soc. 127, 1542 (1980).

54. J. N. Miller, S. A. Schwartz, I. Landau, W. E. Spicer, B. DeMichellis, I. Abbati, and L. Braincovich, J. Vac. Sci. Technol. 17, 920 (1980).

55. R. D. Grinthal, J. Elecrochem. Soc. 107, 59 (1960).

56. I. Binder, J. Amer. Ceram. Soc. 43, 287 (1960).

57. B-Y. Tsaur and L. S. Hung, Appl. Phys. Lett. 37, 922 (1980).

58. J. A. Knapp, S. T. Picraux, C. S. Wu and S. S. Lau, J. Appl. Phys. 58(10), 3747 (1985).

59. J. E. Baglin, F. d'Heurle, and C. S. Petersson, Appl. Phys. Lett 36(7), 594 (1980).

60. J. E. Baglin, F. d'Heurle, and C. S. Petersson, J. Appl. Phys. 52(4), 2841 (1981).

61. J. R. Waldrop, Appl. Phys. Lett. 46(9), 864 (1985).

62. J. H. Weaver, M. Grioni, J.J. Joyce and M. del Giudice, Phys. Rev. B 31(8), 5290 (1985).

63. M. Grioni, M. del Giudice, J.J. Joyce and J. H. Weaver, J. Vac. Sci. Technol. A 3(3), 907 (1985).

64. M. Grioni, J.J. Joyce and J. H. Weaver, Phys. Rev. B 32(2), 962 (1985).

65. J. Nogami, M. D. Williams, T. Kendelewicz, I. Lindau and W. E. Spicer, J. Vac. Sci. Technol. A 4(3), 808 (1986).

66. W. E. Spicer, N. Newman, T. Kendelewicz, W. G. Petro, M. D. Williams, C. E. McCants and I. Lindau, J. Vac. Sci. Technol. B 3(4), 1178 (1985).

67. W. E. Spicer, I. Lindau, P. Skeath, C. Y. Su and P. Chye, Phys. Rev. Lett. 44(6), 420 (1980).

68. W. E. Spicer, I. Lindau, P. Skeath and C. Y. Su, J. Vac. Sci. Technol. 17(5), 1019 (1980).

69. J. L. Freehouf and J. M. Woodall, Appl. Phys. Lett. 39(9), 727 (1981).

70. L. J. Brillson, Surface Science Reports 2, 123 (1982).

71. G. V. Samsonov and I. M. Vinitskii, Handbook of Refractory Compounds (IFI/Plenum Press, New York, 1980).

72. V. S. Neshpor and G. V. Samsonov, Zh. Prikl. Khim. 33(5), 993 (1960).

73. V. S. Neshpor and G. V. Samsonov, Zh. Prikl. Khim. 36(5), 1139 (1963).

74. S. S. Lau, C. S. Pai, C. S. Wu, T. F. Kuech and B. X. Liu, Appl. Phys. Lett. 41(7), 77 (1982).

75. C. S. Wu, S. S. Lau, T. F. Kuech and B. X. Liu, Th. Sol. Films 104, 175 (1983).

76. J. A. Knapp, S. T. Picraux, C. S. Wu and S. S. Lau, Appl. Phys. Lett. 44(8), 747 (1984).

77. I.C. Cheng, S.S. Lau, R. D. Thompson, K.N. Tu, Mat. Res. Soc. Symp. Proc. 25, 39 (1984).

78. H. V. Suu, G. Pető, G. Mezey, F. Paszti, E. Kotai, M. Fried, A Manuaba, E. Zsoldos and J. Gyulai, Appl. Phys. Lett. 48, 437 (1986).

79. C-J. Youn, K. Jungling and W. W. Grannemann, J. Vac. Sci. Technol. A 6(4), 2474 (1988).

80. A. Raman, Trans. Indian Inst. Met. 21(4), 5-8 (1968).

81. I. Mayer, E. Yanir, and I. Shidlovsky, Inorg. Chem. 6(4), 842 (1967).

82. A. Brown, Acta Cryst. 14, 860 (1961).

83. J. A. Perri, E. Banks, and B. Post, J. Phys. Chem. 63, 2073 (1959).

84. A. G. Tharp, J. Phys. Chem. 66, 758 (1962).

85. I. P. Mayer, E. Banks, and B. Post, J. Phys. Chem. 66, 693 (1962).

86. J. A. Perri, I. Binder, and B. Post, J. Phys. Chem. 63, 616 (1959).

87. C. E. Lundin, "A structural survey of the heavy rare earth silicides", in Rare Earth Research, edited by E. V. Kleber (Macmillan, New York, 1961), p.306.

88. A. Iandelli, A. Palenzona, and G. L. Olcese, J. Less Comm. Met. 64, 213 (1979).

89. L. C. Feldman and J. W. Mayer, Fundamentals of Surface and Thin Film Analysis (North-Holland, New York, 1986).

90. H. Iwasaki, R. Nishitani and S. Nakamura, Japan. J. Appl. Phys. 17, 1519 (1978).

91. R. Bellman, R. E. Kalaba, and J. A. Lockett, Numerical Inversion of the Laplace Transform (Elsevier, New York, 1966).

92. T. D. Bussing and P. H. Holloway, J.Vac.Sci.Technol. A 3, 1973 (1985).

93. B. L. Henke, Phys Rev. A 6, 94 (1972).

94. W. A. Fraser, J. A. Florio, W. N. Delgass and W. D. Robertson, Surface Sci. 36, 661 (1973).

95. C. S. Fadley, R. J. Baird, W. Siekhaus, T. Novakov and S. A. L. Bergstrom, J. Electron Microsc. 4, 93 (1974).

96. J. M. Hill, D. G. Royce, C. S. Fadley, L. F. Wagner, and F. J. Grunthaner, Chem. Phys. Lett. 44, 225 (1976).

97. S. Hofmann and J. M. Sanz, J. Trace and Microprobe Tech. 1, 213 (1982-83).

98. S. Hofmann and J. M. Sanz, Surf. and Interf. Anal. 6, 75 (1984).

99. C. S. Fadley, Prog. in Sol. St. Chem. 11, 265 (1976).

100. W. F. Egelhoff, J. Vac. Sci. Tech. A 3, 1511 (1985).

101. R. Kelly, Surf. and Interf. Anal. 7, 1 (1985).

102. R.-S. Li, T. Koshikawa and K. Goto, Surf. Sci. 121, L561 (1982).

103. M. T. Anthony and M. P. Seah, J. Electron Spectrosc. Related Phenomena 32, 73 (1983).

104. C. C. Chang, "Analytical Auger Electron Spectroscopy", in Characterization of Solid Surfaces, edited by P. F. Kane and G. G. Larrabee (Plenum Press, New York, 1974), Chapt. 20, p.509.

105. P. H. Holloway, in Scanning Electron Microscopy/1982, edited by O. Johari (SEM, AFM O'Hare, Illinois, 1982), vol. 1, p.361.

106. P. H. Holloway, Surf. Sci. 66, 479 (1977).

107. S. Mroczkwski and Lichtman, Surf. Sci. 131, 159 (1983).

108. L. E. Davis, N. C. MacDonald, P. W. Palmberg, G. E. Riach and R. E. Weber, Handbook of Auger Electron Spectroscopy, 2nd Edn. (Perkin Elmer Corp., Eden Prairie, Minnesota, 1978).

109. H. J. Mathieu and D. Landolt, Surf. Interf. Anal. 3, 153 (1981).

110. P. M. Hall and J. M. Morabito, Surf. Sci. 83, 391 (1979).

111. W. Reuter, "Ionization function and its application to the electron probe analysis of thin films", in Proc. 6th Intern. Conf. on X-ray Optics and Microanalysis, edited by G. Shinoda, K. Kohra and T. Ichinokawa (Univ. of Tokyo, Tokyo, 1972), p.121.

112. M. Prutton and M. M. El Gomati, Surf. Interf. Anal. 9, 99 (1986).

113. D. R. Penn, J. Electron Spectrosc. Related Phenomena 9, 29 (1976).

114. M. P. Seah and W. A. Dench, Surf. Interf. Anal. 1, 2 (1979).

115. C. J. Powell, N. E. Erickson, and T. E. Madley, J. Electron Spectrosc. Related Phenomena 25, 87 (1982).

116. Th. Wirth, M. Procop and H. Lange, Surf. Interf. Anal. 8, 7 (1986).

117. JCPDS file No. 9-91, Joint Committee on Powder Diffraction Standards (JCPDS International Centre for Diffraction Data, Swarthmore, Pennsylvania, 1979).

118. R. C. Weast, ed., CRC Handbook of Chemistry and Physics, 66th Edition (CRC Press Inc., Boca Raton, Florida, 1986).

119. H. Poppa and L. Cota-Araiza, Thin Solid Films 115, 217 (1984).

120. I. Ohdomari and K. N. Tu, Appl. Phys. 51(7), 3735 (1980).

121. R. D. Thompson and K. N. Tu, J. Appl. Phys. 53, 4285 (1982).

122. A. K. Sinha, J. Electrochem. Soc. 120, 1967 (1973).

123. T. D. Bussing and P. H. Holloway, J. Vac. Sci. Tech. B 6(5), 1514 (1988).

124. K. N. R. Taylor and M. I. Darby, Physics of Rare Earth Solids (Chapman and Hall LTD, London, 1972).

125. P. Wacter, CRC Critical Reviews in Solid St. Sciences (1972) p. 189.

126. A. Hasegawa and A. Yanase, J. Phys. Soc. of Japan 42(2), 492 (1977).

127. R. P. Elliot, Constitution of Binary Alloys, First Supplement (McGraw-Hill, New York, 1958).

128. G. Rajeswaran, W. A. Anderson, M. Jackson, and M. Thayer, Thin Solid Films 104, 351 (1983).

129. R. D. Frampton, E. A. Irene, and F. M. d'Heurle, J. Appl. Phys. 59(3), 978 (1986).

130. S. P. Tobin, Final Report SAND88-7033 (Sandia National Laboratories, Albuquerque, New Mexico, November 1988).

BIOGRAPHICAL SKETCH

Mr. Bussing was born at Ft. Bell, Bermuda, in 1948 and was raised in the itinerant lifestyle associated with his father's career as an Air Force officer. After graduating from high school in Glasgow, Montana, he attended Harvard University, receiving the degree of Bachelor of Arts in applied mathematics in 1969.

After pursuing postbaccalaureate studies in biology and chemistry at the University of Minnesota, he relocated to Montgomery Center, Vermont, as a partner in a restaurant and property development project. He continued to pursue opportunities in the building trades with both independent and salaried positions in Vermont and other locations, eventually relocating to Florida in 1982.

A continuing interest in scientific subjects, along with a conviction that the development of solar energy conversion as a practical alternative is key to our nation's future, led Mr. Bussing to enroll in the PhD program in the department of Materials Science and Engineering at the University of Florida.

I certify that I have read this study and that in my opinion it conforms to acceptable standards of scholarly presentation and is fully adequate, in scope and quality, as a dissertation for the degree of Doctor of Philosophy.

Paul H. Holloway, Chair
Professor of Materials
Science and Engineering

I certify that I have read this study and that in my opinion it conforms to acceptable standards of scholarly presentation and is fully adequate, in scope and quality, as a dissertation for the degree of Doctor of Philosophy.

Robert E. DeHoff
Professor of Materials
Science and Engineering

I certify that I have read this study and that in my opinion it conforms to acceptable standards of scholarly presentation and is fully adequate, in scope and quality, as a dissertation for the degree of Doctor of Philosophy.

Rolf E. Hummel
Professor of Materials
Science and Engineering

I certify that I have read this study and that in my opinion it conforms to acceptable standards of scholarly presentation and is fully adequate, in scope and quality, as a dissertation for the degree of Doctor of Philosophy.

Kevin S. Jones
Assistant Professor of
Materials Science and
Engineering

I certify that I have read this study and that in my opinion it conforms to acceptable standards of scholarly presentation and is fully adequate, in scope and quality, as a dissertation for the degree of Doctor of Philosophy.

Gar B. Hoflund
Professor of Chemical Engineering

This dissertation was submitted to the Graduate Faculty of the College of Engineering and to the Graduate School and was accepted as partial fulfillment of the requirements for the degree of Doctor of Philosophy.

May 1991

for Winfred M. Phillips
Dean, College of Engineering

Madelyn M. Lockhart
Dean, Graduate School